Supporting Information

Local Structure and Bonding of Carbon Nanothreads Probed by High-Resolution Transmission Electron Microscopy

Stephen J. Juhl,[1] Tao Wang,[2] Brian Vermilyea,[2] Xiang Li,[1] Vincent H. Crespi,[1,2,3,4] John V. Badding,[1,2,3,4] and Nasim Alem[3,4,*]

[1]Department of Chemistry, Pennsylvania State University, University Park, Pennsylvania 16802, USA
[2]Department of Physics, Pennsylvania State University, University Park, Pennsylvania 16802, USA
[3]Department of Material Science and Engineering, Pennsylvania State University, University Park, Pennsylvania 16802, USA
[4]Materials Research Institute, Pennsylvania State University, University Park, Pennsylvania 16802, USA
*Correspondence to: nua10@psu.edu

1. Materials and Methods

Nanothread TEM samples were prepared by crushing nanothreads in an agate mortar followed by dispersion in cyclohexene and drop-casting onto copper TEM grids with lacey carbon support film (Electron Microscopy Sciences, LC325-Cu). EELS spectra were acquired with an FEI Tecnai G2 20 XTWIN microscope operated at 200 kV in diffraction mode with a collection semi-angle of 2.695 mrads. The collection angle was chosen to optimize the signal collection angle for the carbon K-edge at 200 kV (characteristic angle ~0.71 mrad). The optimum signal-to-background ratio for EELS ionization edges is three times the characteristic angle of the edge (in this case ~2.13 mrads). The fractions of sp^2 and sp^3 carbon were calculated using the two-window method with a glassy carbon standard (Figure S1).[1] We assume no *sp* carbon is present in the sample because it is unlikely for bond order to increase under high pressure. Therefore, the sp^2 and sp^3-content can be calculated directly from the relative areas of the π^* peak to the σ^* peak. The EELS spectrum shown in Figure 1 was smoothed using the Savitzky-Golay method using a 2nd-order polynomial fit over 81 points in IGOR Pro (WaveMetrics, Inc.). The unsmoothed EELS spectrum is also shown in Figure S1. Electron diffraction patterns were collected on an FEI Talos F200X microscope operated at 200 kV using a Gatan double-tilt holder. The dose rate was kept at less than 0.01 e/Å^{2}s by spreading the electron beam at low magnifications and using a selected-area aperture to isolate a single nanothread particle. The acquisition time was increased to the maximum of 55 seconds to increase the intensity of the high-order reflections. Measurements of the electron diffraction patterns and HREM image FTs were made in the Gatan Microscopy Suite® software using scripts developed by Mitchell et al.[1] (Figure S5 and Figure S10). The $\langle 10\bar{1}0 \rangle$ were compared with various models of nanothreads and indexing of the diffraction patterns confirmed the pseudohexagonal crystal structure (Figures S2–S5). We collected TEM images using an FEI Titan^3 G2 microscope, equipped with double aberration correction and a gun monochromator, operated at 80 kV for

HREM imaging (Figures S32–S34). The electron dose in electrons/pixel was calculated from the pixel values after calibration of the Gatan UltraScan 1000 camera. The dose was adjusted by operating the electron gun monochromator over vacuum and changing the position of the monochromator slit to select a part of the beam with low electron density. Autocorrelation of an image of the nanothreads viewed along the [0001] zone axis (Figure S9) was performed in FIJI.[2] Measurements of the $\langle 10\bar{1}0 \rangle$ interplanar spacings were taken from the Fourier transform (Figure S10) of an image of the nanothreads in the [0001] orientation (Figure 4d). The total dose of 150 e/Å^2 was found to expand the $\langle 10\bar{1}0 \rangle$ interplanar spacings to 6.4 Å, and therefore a lower dose was employed for other HREM images.

2. Modeling and Simulations

Axially-ordered nanothread models (Figure S2) – which were previously enumerated with a constraint of at most two benzene rings in the topological unit cell and structurally optimized by first-principles calculations[3] – were originally hexagonally packed (with registry or disregistry) into a single supercell of size 4×4×y, where y is the number of nanothread axial unit cells (y=1 for threads with Z>6, otherwise y=3, where Z is the number of progenitor benzene rings in the unit cell) using a self-coded python program and fully relaxed at a classical MD level with the AMBER empirical force field implemented in LAMMPS.[4-5] We also generated on-thread-disordered nanothreads by randomizing the endpoints of the polymerization bonds between constituent phenyl rings (through Stone-Wales transformations) in a long axial supercell while maintaining saturation and nanothread class (i.e. the number of covalent bonds between successive rings, here either class 2, which is 2 bonds down/up and 4 bonds up/down, or class 3, which is 3 bonds up/down). This optionally imposes a constraint for the inter-ring bonding pattern to be consistent with [4+2] cycloaddition, thus yielding four exemplars of on-thread disorder, written as "disordered class 2 and class 3" and "disordered [4+2] class 2 and class 3" (Figure S2).[6] These on-thread-disordered models have no axial periodicity over the 2.71–2.93 nm length of the simulation cell.

We performed electron diffraction simulations on a variety of nanothread structures (Figure S2) with packing registry or disregistry in the [0001] (Figures S6–S8) or $[10\bar{1}0]$ orientations (Figures S11–S13). The electron diffraction simulations were performed using the SingleCrystal™ and CrystalMaker™ software. Electron diffraction simulation parameters were set to 1000 mm camera length and 100-nm thickness (the maximum thickness measured by EELS plasmon-to-zero-loss peak ratio) to mimic experiment as closely as possible. The number of simulated reflections was capped at 1 million because of computational limitations, but the Q-range of the simulations was sufficient (>1 Å^{-1}) for comparison to experimental diffraction patterns. The d-spacings of the $\{10\bar{1}0\}$ reflections measured from experimental (Figure S5) and simulated (Figures S6–S8) diffraction patterns are compared in Figures S3–S4. Layer lines are observed in the diffraction simulations of nanothreads with packing disregistry (Figures S11–S13) as

well as in the experimental data (Figure S15). We illustrate the origin of layer lines in a familiar example by simulating the electron diffraction pattern of B-DNA and comparing it with the well-known x-ray diffraction pattern by Rosalind Franklin (Figure S14). We used the Scherrer equation to estimate the nanothread domain length associated with the experimentally observed layer lines (Figure S15) and confirmed these domain lengths by simulating electron diffraction patterns of isolated nanothreads with varying segment lengths (Figure S16).

TEM image simulations were performed on a variety of nanothread models packed in registry or disregistry using the MacTempasX software (Figures S17–S26). In view of the beam sensitivity of nanothreads, during experiments we had only enough time to find the Scherrer defocus and image the samples. Therefore, it was not possible to determine the absolute defocus values of the experimental images. Nonetheless, we can be certain that the defocus was positive because it was set this way in conjunction with a –15 nm C3 value to produce white-atom contrast in the HREM images. Therefore, we chose to simulate a range of positive defocus values from 0 to +40 nm. For each simulation, a supercell consisting of a 4×4×y array of threads was considered (y is the number of axial thread unit cells), as indicated in Figures S17–S26. The thicknesses used for the simulations of the nanothread supercells ranged from ~2.5 nm (single supercell) to ~100 nm (repeated supercell) for the $[10\bar{1}0]$ and from ~5 nm (single supercell) to ~100 nm (repeated supercell) for [0001]. Therefore, the smallest supercell thickness is equivalent to the dimension of one supercell and the largest thickness is equal to many supercells stacked to reach the maximum thickness measured by EELS. TEM image simulations using these defocus values and thicknesses show a pseudohexagonal packing structure and beading along the nanothread axis (Figures S17–S26) that are similar to experimental images (Figures S32–S34).

The MacTempasX software utilizes the multi-slice approach for TEM simulations and achieves the desired simulation thickness by repeating the unit cell in the assigned direction (in this case, the unit cell is equivalent to one supercell with a 4×4×y array of threads). This presents a challenge for simulation of packing disregistry over large thicknesses, because the repetition of the supercell inherently creates supercell-to-supercell registry. Thus, the only method to simulate "complete" packing disregistry is to generate a supercell (unit cell) that has the same dimensions as the desired simulation. We have generated a single large supercell (128×4×1) of stiff-chiral-3 nanothreads with packing disregistry that has thickness in the $[10\bar{1}0]$ direction (87.4 nm) similar to the experimentally-measured thickness of nanothread particles (inter-thread interactions were not structurally relaxed in this model for reasons of computational cost). In Figure S31, we show TEM image simulations with thickness = 87.4 nm and defocus = 0–40 nm for this large supercell and compare with image simulations of smaller supercells that are exact fractions of the 128×4×1 supercell (i.e. 64×4×1, 32×4×1, and 16×4×1). As Figure S31 indicates, while supercell-to-supercell registry along the thickness of the samples promotes

beading, we still observe beading in TEM image simulations for some defocus values even in cases of complete disregistry. Therefore, these simulations do not afford conclusions as to the amount of registry that is present in the sample.

To learn about the fine structure of the nanothreads, we compare the beading observed in simulated versus experimental HREM images of nanothreads (Figures S27–S30). The experimental HREM images have a pixel size of ~1 $Å^2$ whereas the simulated TEM images have a pixel size of ~10 pm^2. To facilitate comparisons of the simulated and experimental images, the simulated images were binned to ~1 $Å^2$ pixel size (Figures S27–S28). The range of inter-bead distances measured in TEM image simulations of nanothread models with packing disregistry is similar to the range of inter-bead distances measured in experimental images (Figures S27–S30).

3. Supporting Figures

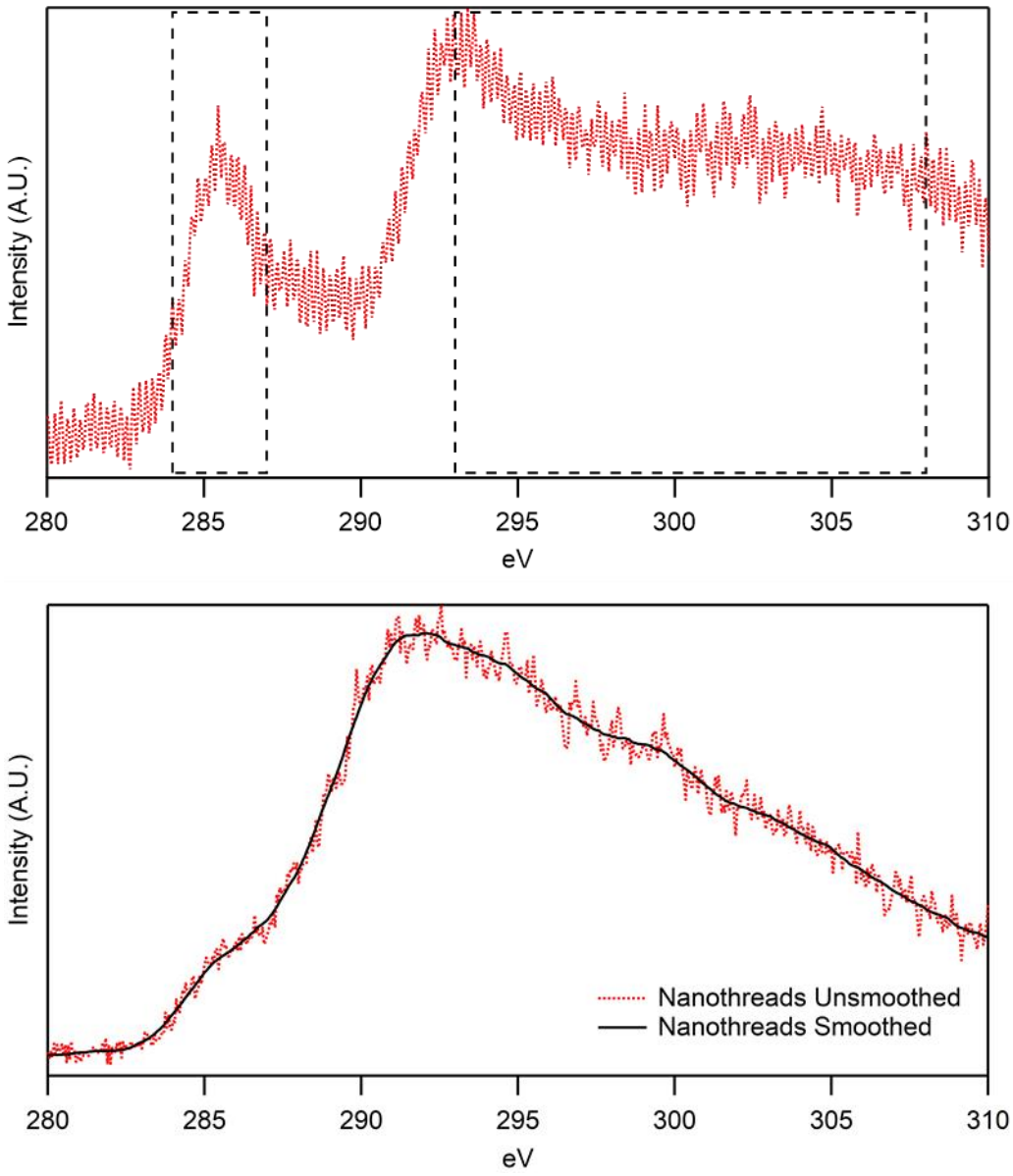

Figure S1. EELS spectra of the carbon K-edge of glassy carbon (top) and nanothreads (bottom). Both spectra are shown after background subtraction by power law fitting and subsequent deconvolution to remove plural scattering. The π^* and σ^* windows that were used to integrate the spectra for the determination of sp^2/sp^3 ratios are overlaid on the glassy carbon spectrum, used as an sp^2 carbon standard. The nanothread EELS is smoothed by an 81-point 2nd-order Savitzky-Golay filter for publication in Figure 1. The unsmoothed and smoothed spectra of nanothreads are overlaid for comparison.

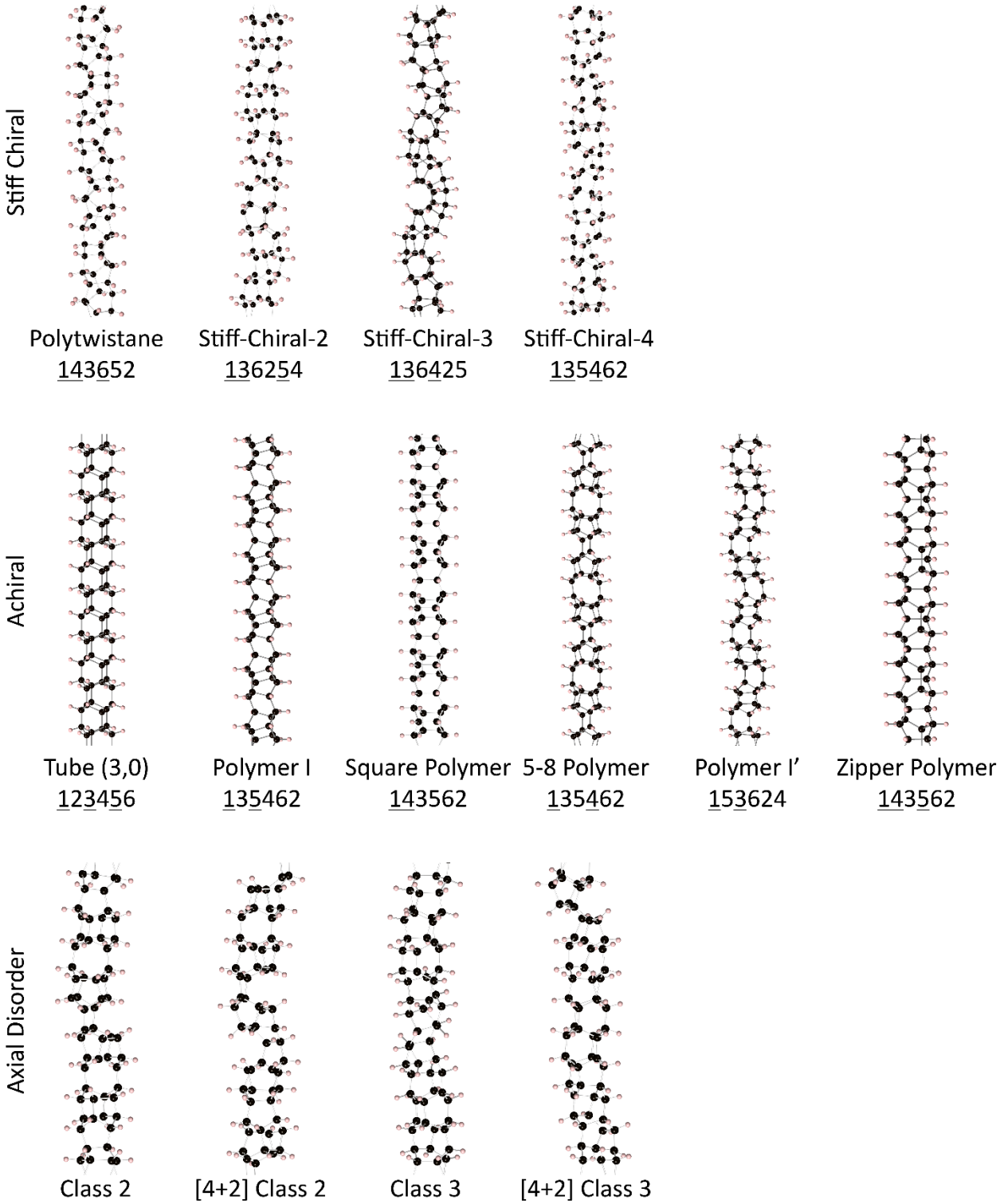

Figure S2. Models of nanothreads sorted into three categories based on their axial structural characteristics: stiff chiral, achiral, or axial disorder. Each structural model is shown approximately 3 nm long, regardless of its axial repeat unit, and is labelled with its conventional name and the numerical nomenclature described by Xu et al.[3]

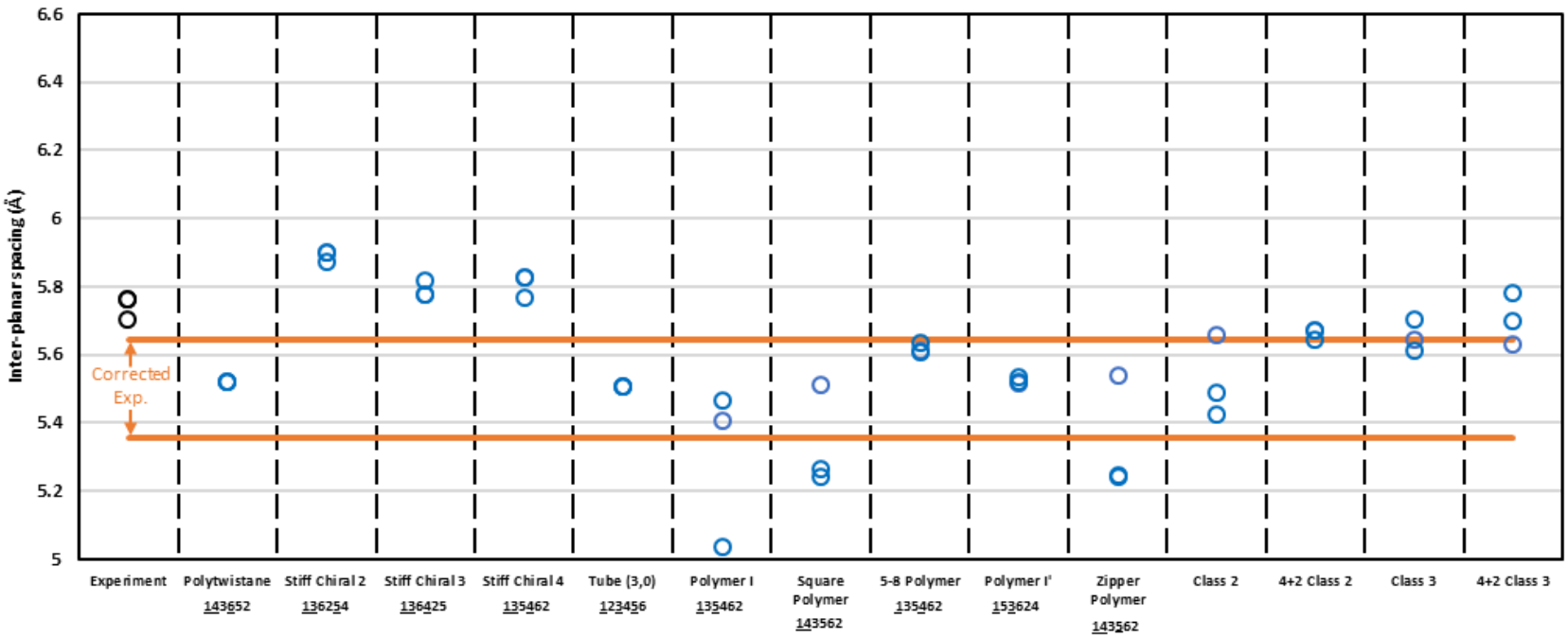

Figure S3. Comparison of $\langle 10\bar{1}0 \rangle$ interplanar spacings from experiment (T = 300 K) and various nanothread models with packing registry (T = 0 K). Black points represent the experimental interplanar spacings determined from SAED. Blue points represent the interplanar spacings measured from simulated [0001] electron diffraction patterns of nanothread models packed in registry at T = 0 K. Considering that there is thermal expansion and beam-induced dilation of the lattice, our experimental measurements from the electron diffraction data will be higher than that extracted from the simulated models. From the previously published XRD diffraction patterns, we estimate a lattice expansion of 1–3% due to the electron beam damage. A thermal expansion of 1-3% from 0 to 300 K was estimated from the thermal coefficients of similar material systems (see Li et al.[7]) and was applied to the experimental electron diffraction data to better compare them with the T = 0 simulations. The upper and lower orange lines show the range of inter-planar spacings for the experimental electron diffraction data after applying correction factors for both thermal and beam-induced expansions (a total of 2–6%). The blue data points that fall within the two orange lines indicate inter-planar spacing consistent with those observed in experiment. Note that the structural models (excluding the last four which are highly disordered) do not include on-thread structural disorder, which would be expected to induce some further lattice dilation and to reduce azimuthal anisotropy (i.e. differences between the Friedel pairs).

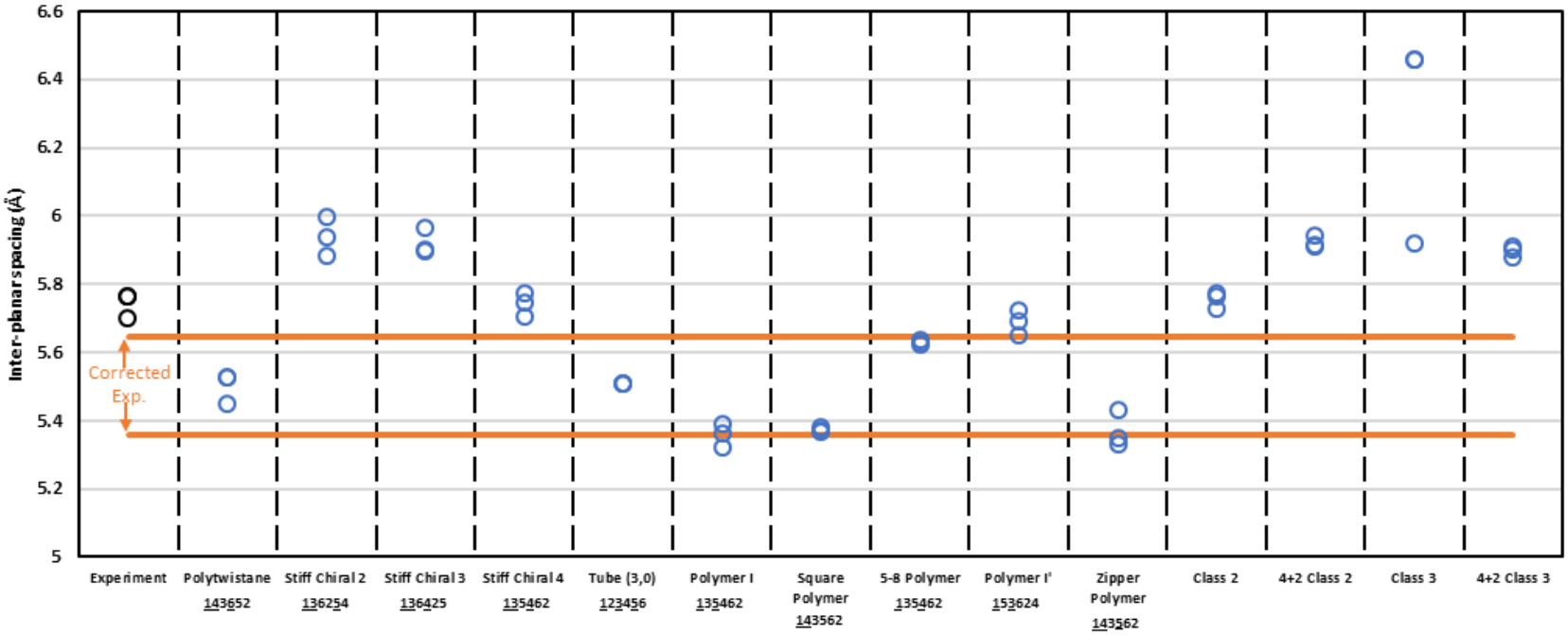

Figure S4. Comparison of $\langle 10\bar{1}0 \rangle$ interplanar spacings from experiment (T = 300 K) and various nanothread models with packing disregistry within 4×4×y supercells (T = 0 K). Black points represent the experimental interplanar spacings determined from SAED. Blue points represent the interplanar spacings measured from simulated [0001] electron diffraction patterns of nanothread models packed in disregistry at T = 0 K. Considering that there is thermal expansion and beam-induced dilation of the lattice, our experimental measurements from the electron diffraction data will be higher than was measured form the simulated models. From the previously published XRD diffraction patterns, we estimate a lattice expansion of 1–3% due to the electron beam damage. A thermal expansion of 1-3% from 0 to 300 K was estimated from the thermal coefficients of similar material systems (see Li et al.[7]) and was applied to the experimental electron diffraction data to better compare them with the T = 0 simulations. The upper and lower orange lines show the range of inter-planar spacings for the experimental electron diffraction data after applying correction factors for both thermal and beam-induced expansions (a total of 2–6%). The blue data points that fall within the two orange lines indicate inter-planar spacing consistent with those observed in experiment. Note that the structural models (excluding the last four which are highly disordered) do not include on-thread structural disorder, which would be expected to induce some further lattice dilation.

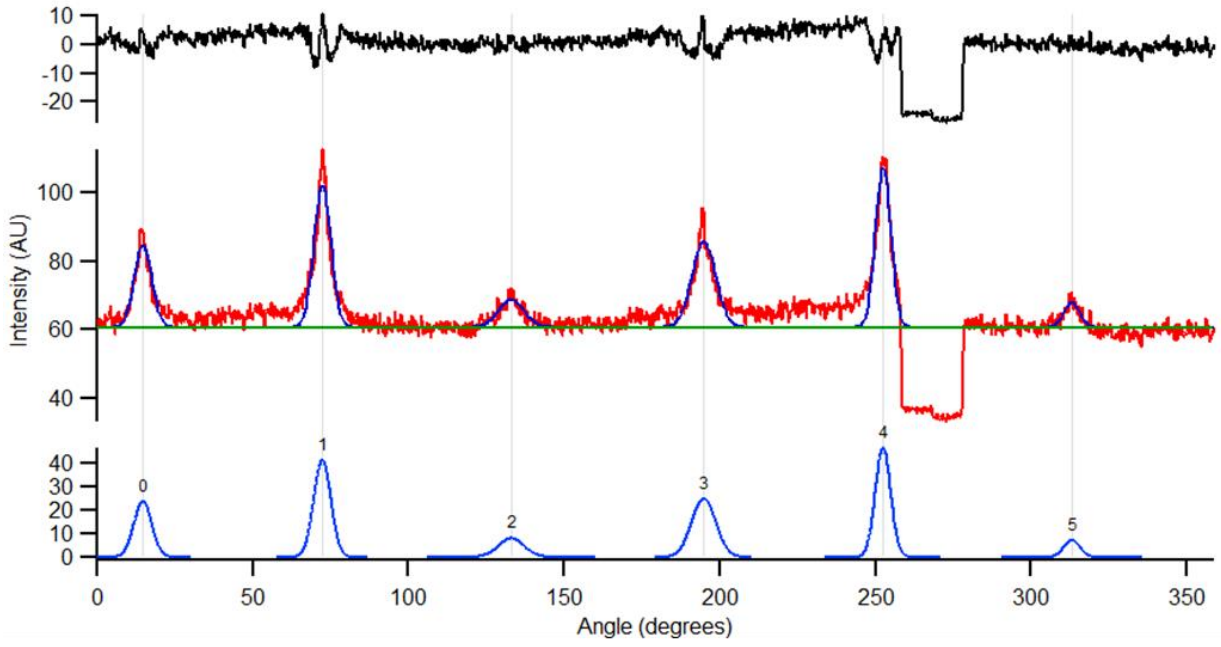

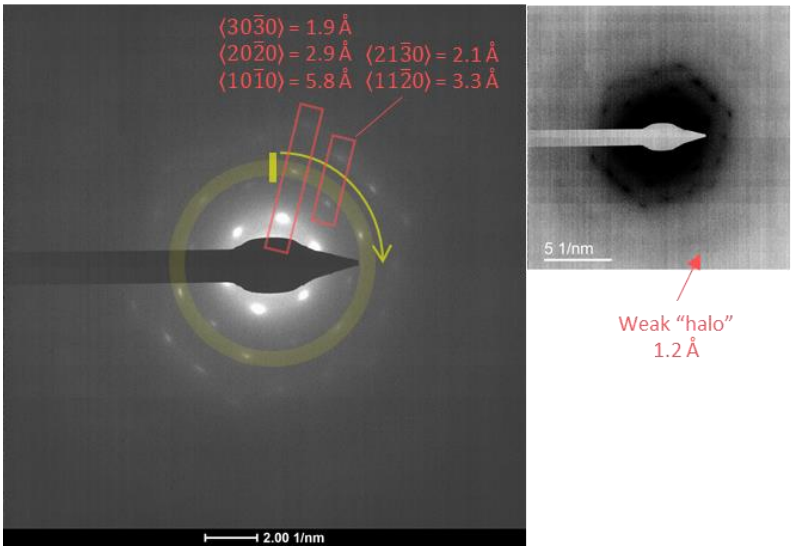

Peak	Location (°)	FWHM (°)	Angle (°)
0	14.68	6.67	61.65
1	72.34	6.41	57.66
2	132.96	9.72	60.62
3	194.84	9.03	61.88
4	252.46	5.80	57.62
5	313.03	6.00	60.57

Figure S5. The angular distribution (arc length) of the {20$\bar{2}$0} reflections in the a-b plane of the [0001] SAED pattern (Figure 4a) is plotted and fit with Gaussian peaks. The spectra show the angular distribution (red) overlaid with the background fit (green) and the Gaussian peak fits (blue). The bottom line shows only the Gaussian peaks (blue) and the top line shows the residual signal (black) after subtracting the background and Gaussians from the angular distribution. The consistent spiked shape of the residual indicates some deviation from a Gaussian profile, but this does not significantly affect the accuracy of the width determination. The SAED pattern shows the starting point (yellow line) and direction of the angular rotation measurement in yellow (as we go around the circumference of the yellow circle), and the interplanar spacing measurements for ⟨10$\bar{1}$0⟩, ⟨11$\bar{2}$0⟩, ⟨20$\bar{2}$0⟩, ⟨21$\bar{3}$0⟩, and ⟨30$\bar{3}$0⟩ in red. The table shows the locations of the center and FWHM of each fitted Gaussian peak as we go around the yellow circle, and the angle between the {20$\bar{2}$0} reflections. The small SAED pattern with inverted contrast reveals the weak diffuse hexagonal diffraction ring at large Q with an interplanar spacing of about 1.2 Å (close to the C–H bond length). This hexagonal envelope of diffuse scattering is consistent with the streaks found between the diffraction spots. These streaks indicate that the nanothreads have packing disregistry.

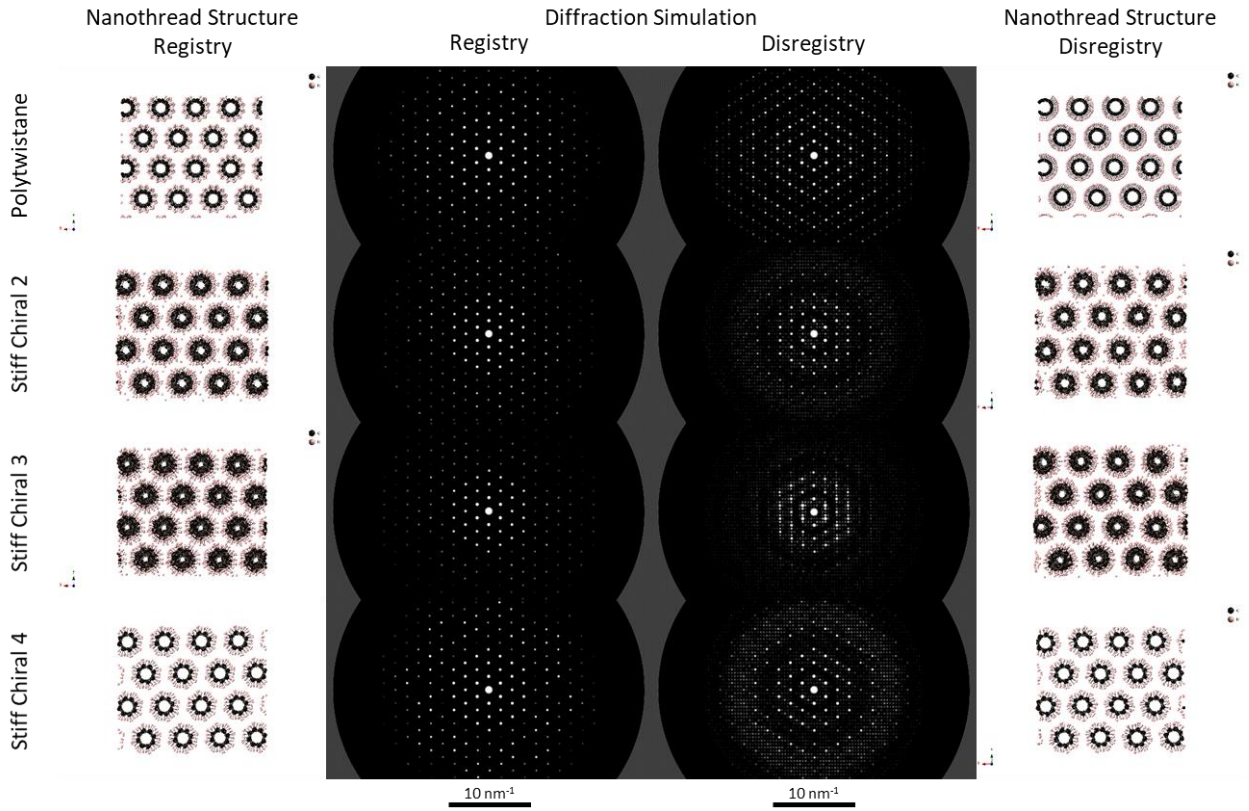

Figure S6. Rendered real-space models (left) and simulated electron diffraction patterns (center, right) along the [0001] direction of polytwistane (14̲36̲52), stiff-chiral-2 (13̲62̲54), stiff-chiral-3 (13̲64̲25), and stiff-chiral-4 (13̲54̲62) nanothreads with packing registry (center) or packing disregistry (right). These nanothread structures are defined as "stiff chiral".[3] We note that all of the stiff-chiral nanothread packings produce a "hexagonal halo" in the simulated [0001] electron diffraction patterns, which is similar to the experimental SAED pattern in Figure 3. Disregistry seems to accentuate the halo. The hexagonal halo is not found in the simulated [0001] electron diffraction patterns of some other nanothread models (Figures S7–S8). By comparing the simulated electron diffraction patterns and the images of the [0001] projection of their models, the source of the hexagonal halo is evidently that the near-circular shape of the individual nanothreads in the [0001] projection does not create preferred orientations in the packing models.

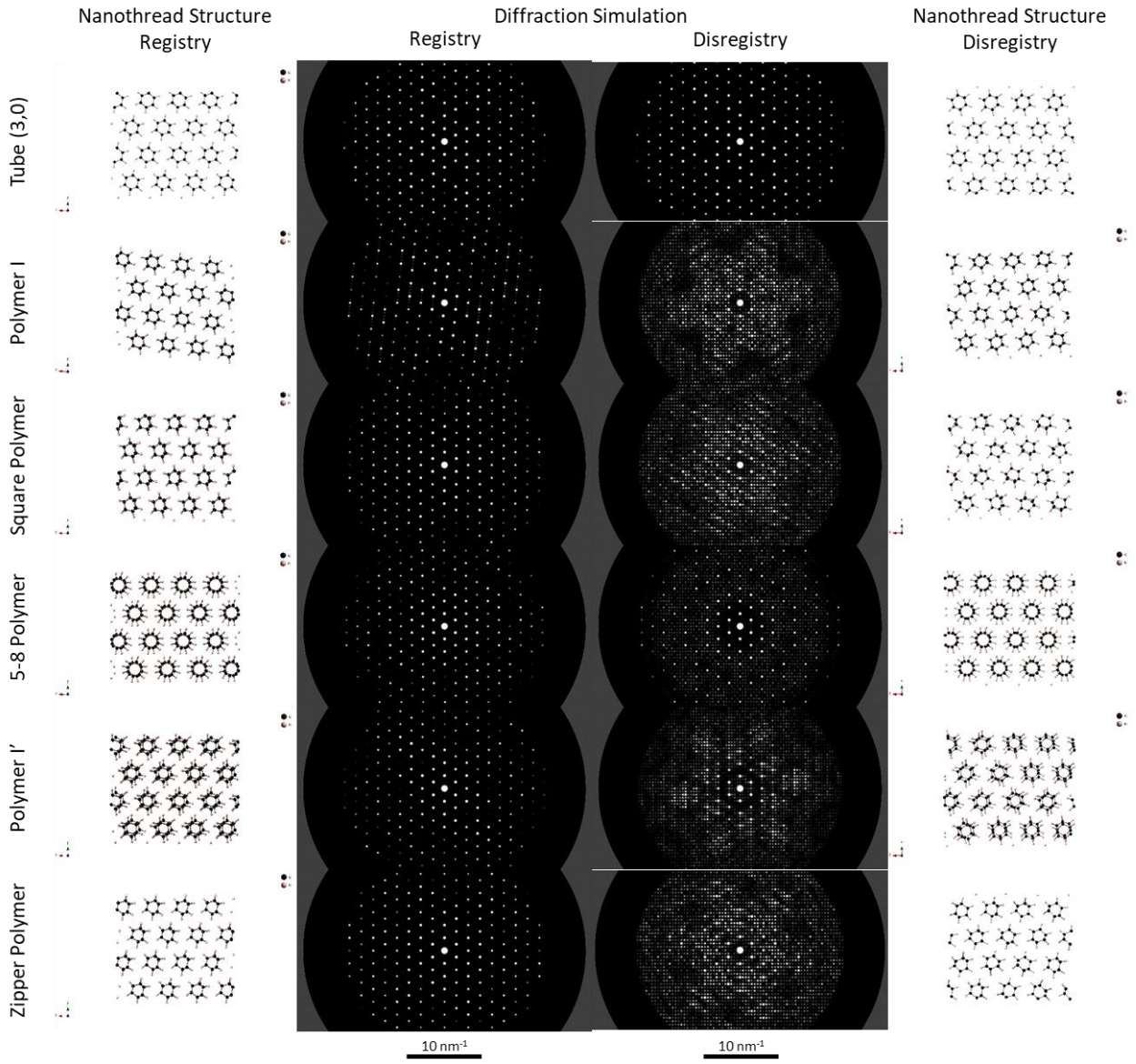

Figure S7. Rendered real-space models (left) and simulated electron diffraction patterns (center, right) along the [0001] direction of tube (3,0) (12345̲6), polymer I (13̲5462), square polymer (14̲3562), 5-8 polymer (13̲54̲62), polymer I' (15̲3̲624), and zipper polymer (14̲3̲5̲62) nanothreads with packing registry (center) or packing disregistry (right). These nanothread structures are achiral.[3] We note that the achiral structures for defect-free threads do not produce a hexagonal halo in the simulated [0001] electron diffraction patterns (with the exception of 5-8 polymer), and instead produce a star-like pattern. The origin of the star appears to be a lower-symmetry ("lumpy") projected shape of the individual nanothreads when viewed in the [0001] direction, which creates a finite set of preferred azimuthal orientations in the packing models. Note that irregular domains along the thread axes (not simulated due to structural complexities) could frustrate the formation of these preferred orientations by interrupting the required coherence in interthread interactions.

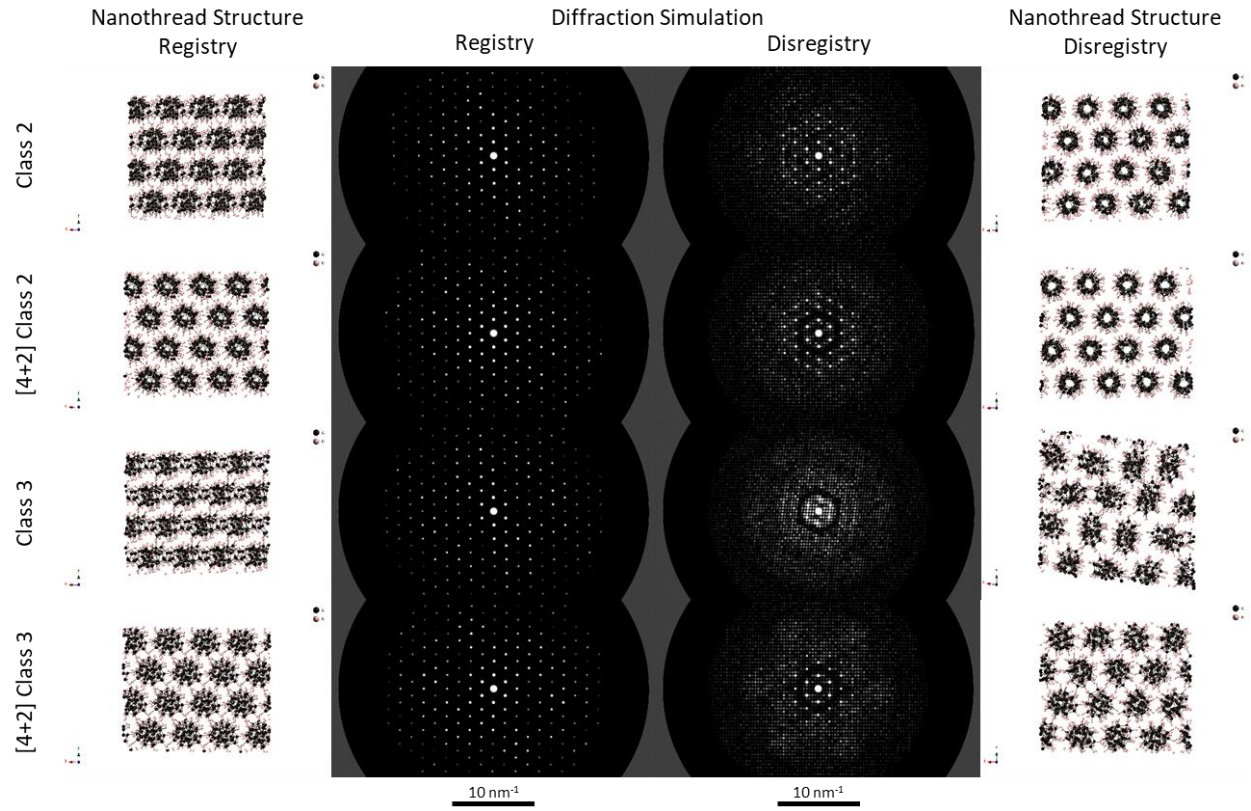

Figure S8. Rendered real-space models (left) and simulated electron diffraction patterns (center, right) along the [0001] of on-thread disordered class 2, [4+2] class 2, class 3, and [4+2] class 3 nanothreads with packing registry or packing disregistry. These axially-disordered diffraction simulations can express either a hexagonal halo or a star-like diffraction pattern depending on the precise disorder realization, but the patterns are generally less distinct than patterns for axially-ordered nanothread models.

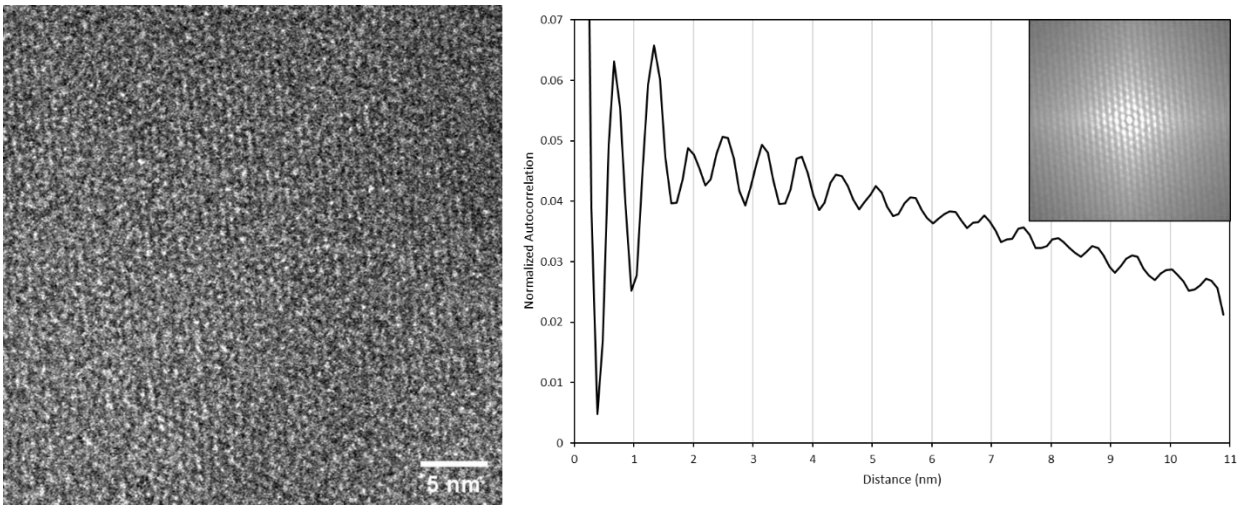

Figure S9. Radially-averaged autocorrelation (right) of the HREM image shown in Figure 4d (left) shows relatively strong autocorrelation to d = 1.3 nm, or the second-nearest thread neighbor. This autocorrelation indicates that nanothreads form well-aligned bundles of approximately 3×3 threads, as demonstrated by the two-point correlation image shown in the inset and the bundle of well-aligned threads outlined in the inset of Figure 4e.

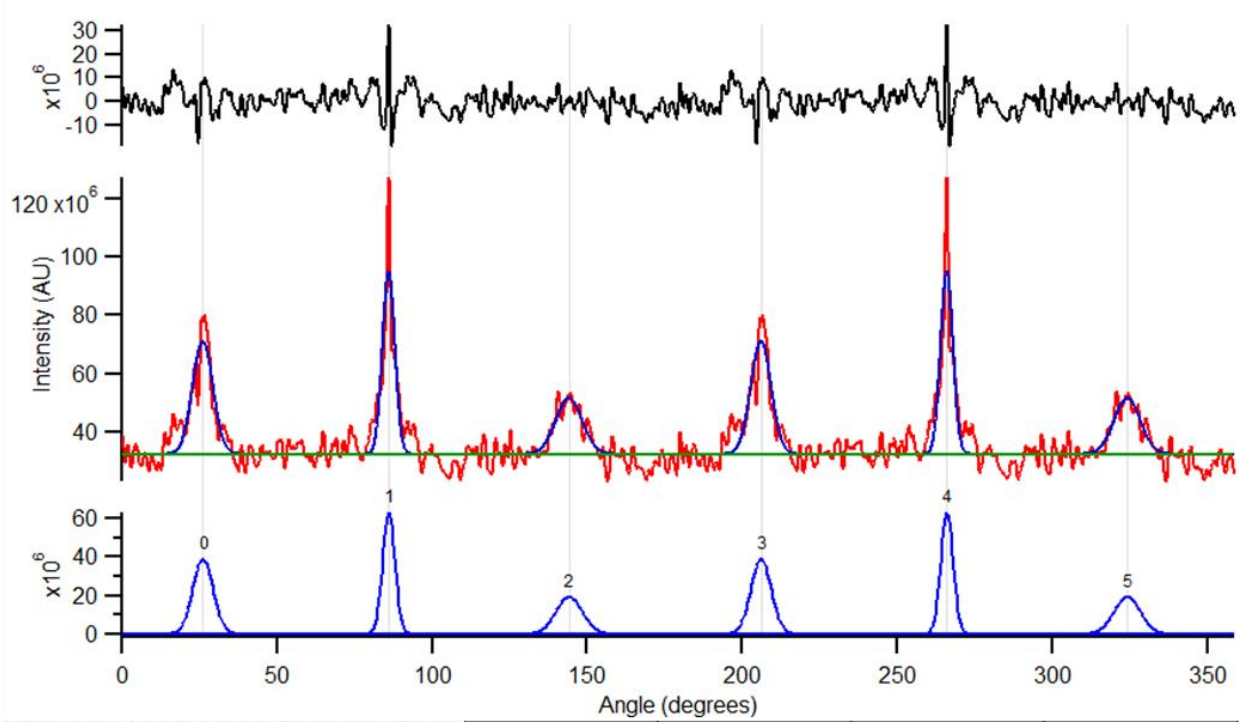

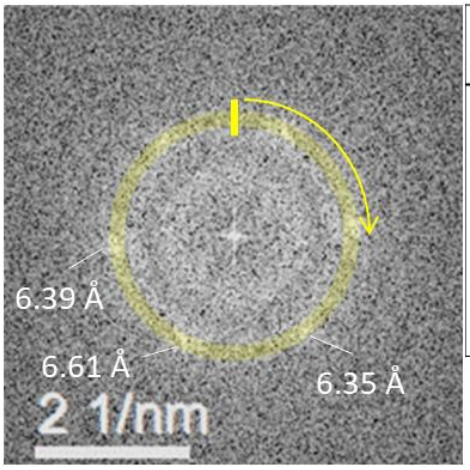

Peak	Location (°)	FWHM (°)	Angles (°)
0	26.11	7.74	61.9
1	86.06	4.69	59.95
2	144.18	10.00	58.12
3	206.14	7.74	61.96
4	266.09	4.69	59.95
5	324.21	10.00	58.12

Figure S10. Angular distribution of Fourier-transform spots from Figure 4d. In Figure 4d, the HREM image along [0001] shows small domains that appear to be separated by areas of slight misorientation. To determine the angle of misorientation in Figure 4d, the angular spread of the Fourier spots from the FT of the HREM image were fit by Gaussian functions. The middle line of the plot shows the raw data (red) overlaid with the background fit (green) and the Gaussian peak fits (blue). The bottom line shows just the Gaussian peaks (blue) and the top line shows the residual signal (black) after subtracting the background and Gaussians from the raw signal. The spiked shape of the residuals indicates some deviation from a Gaussian profile, but this does not significantly affect the accuracy of the width determination. The Fourier transform shows the location and direction of the angular rotation measurement. The table shows the locations of the center and FWHM of each fitted Gaussian peak. The FWHM values from the FT of the HREM image are in good agreement with the FWHM values fitted from the SAED pattern of a different particle (Figure 4a), shown in Figure S5.

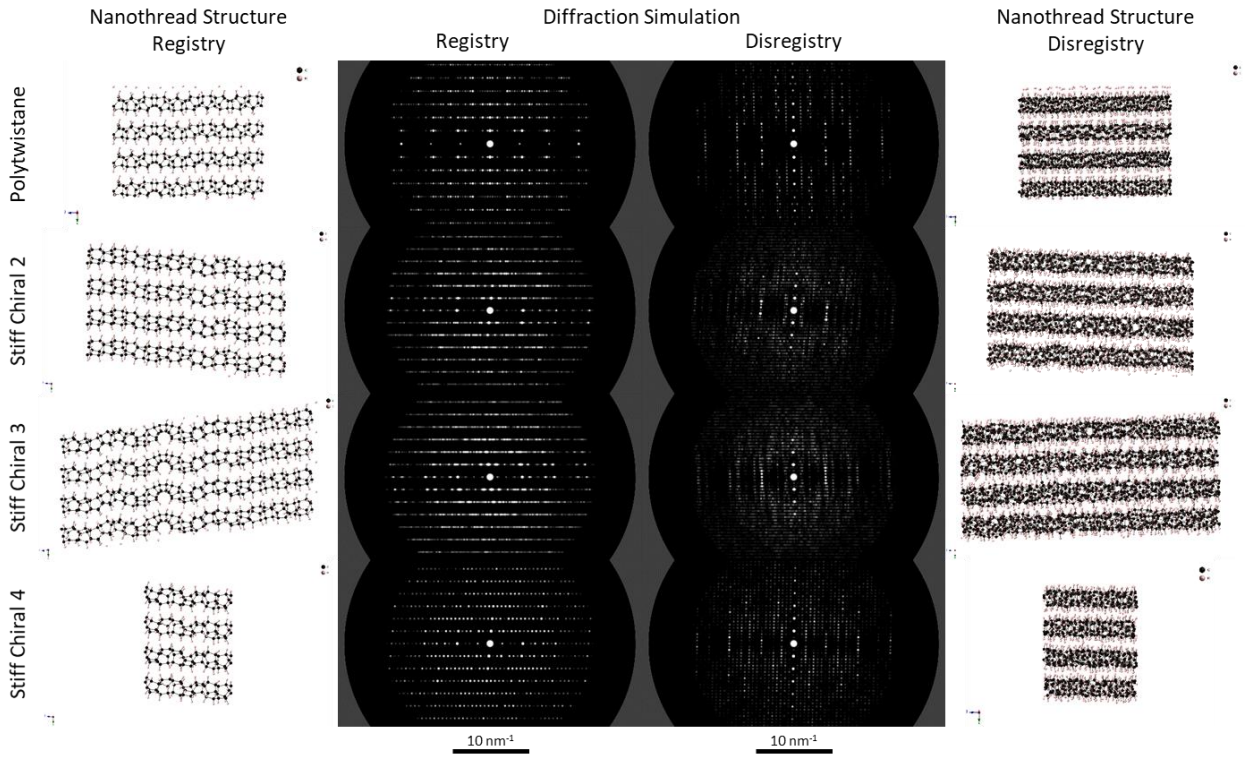

Figure S11. Rendered real-space models (left) and simulated electron diffraction patterns (center, right) viewing along the [10$\bar{1}$0] of polytwistane (14$\underline{3}$6$\underline{5}$2), stiff-chiral-2 (1$\underline{3}$62$\underline{5}$4), stiff-chiral-3 (1$\underline{3}$64$\underline{2}$5), and stiff-chiral-4 (1$\underline{3}$5$\underline{4}$62) nanothreads with either packing registry or packing disregistry. These structures are defined as "stiff chiral".[3] The nanothreads are oriented in the horizontal direction in real space and therefore any layer lines (which are associated with oriented fiber diffraction) should appear nearly perpendicular to the horizontal axis. Stiff chiral threads with packing registry (center left) show equally-spaced horizontal rows of dense spots whose inter-row spacing is associated with thread packing, but no layer lines. Models with packing disregistry (center right) show many weak and tightly-spaced reflections that approximate diffuse scattering, with a concentration along layer lines similar to those observed in experimental diffraction patterns.

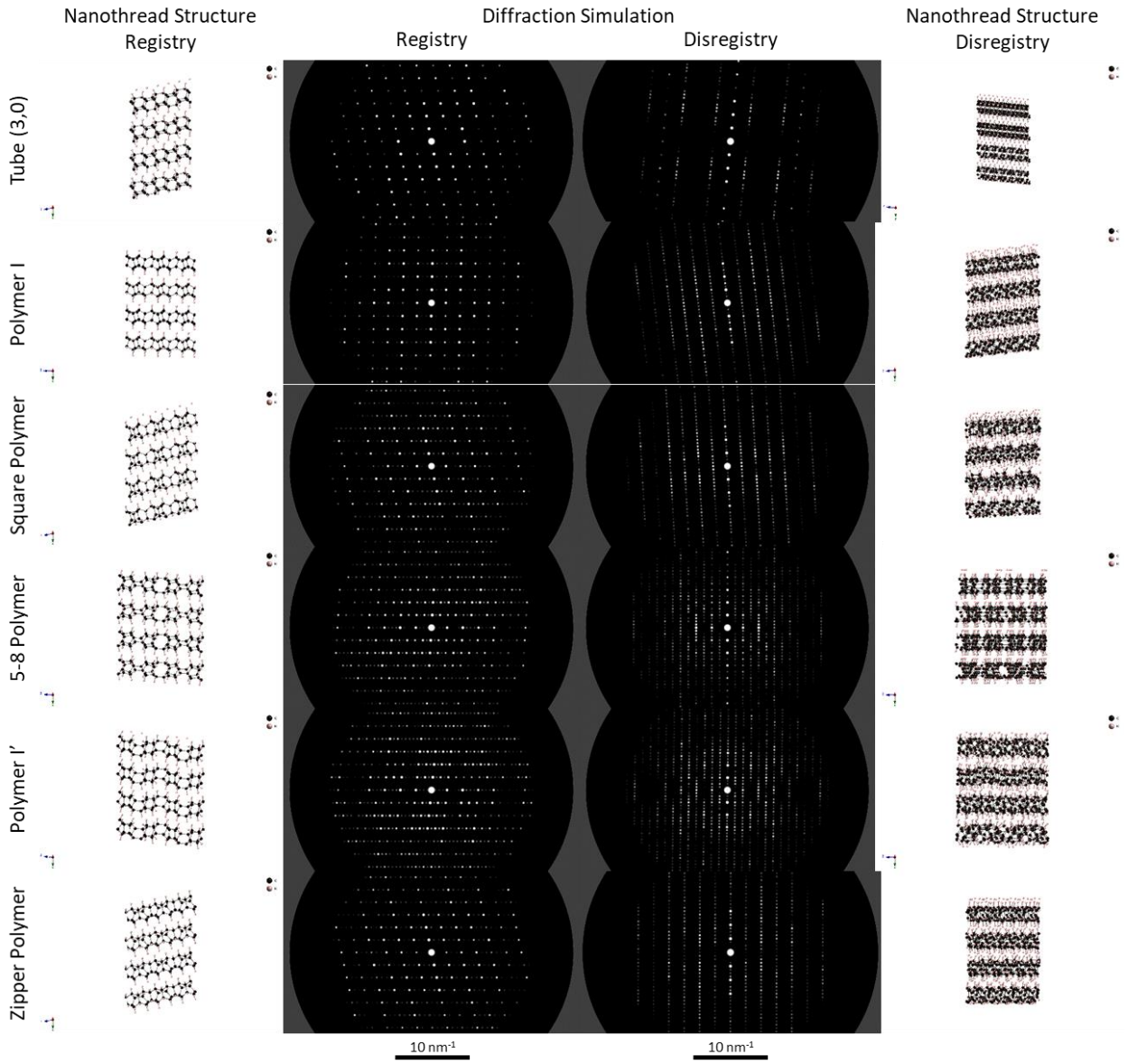

Figure S12. Rendered real-space models (left, right) and simulated electron diffraction patterns (center) viewing along the [10$\bar{1}$0] of achiral nanothreads tube (3,0) (12$\underline{3}$4$\underline{5}$6), polymer I (1$\underline{3}$5462), square polymer (1$\underline{4}$3562), 5-8 polymer (1$\underline{3}$5$\underline{4}$62), polymer I' (1$\underline{5}$3624), and zipper polymer (1$\underline{4}$3$\underline{5}$62) with either packing registry or packing disregistry. The models with packing registry exhibit a regular array of reflections with no distinct layer lines, whereas models with packing disregistry show many weak and tightly-spaced reflections that approximate diffuse scattering, but with a concentration along layer lines similar to those observed experimentally.

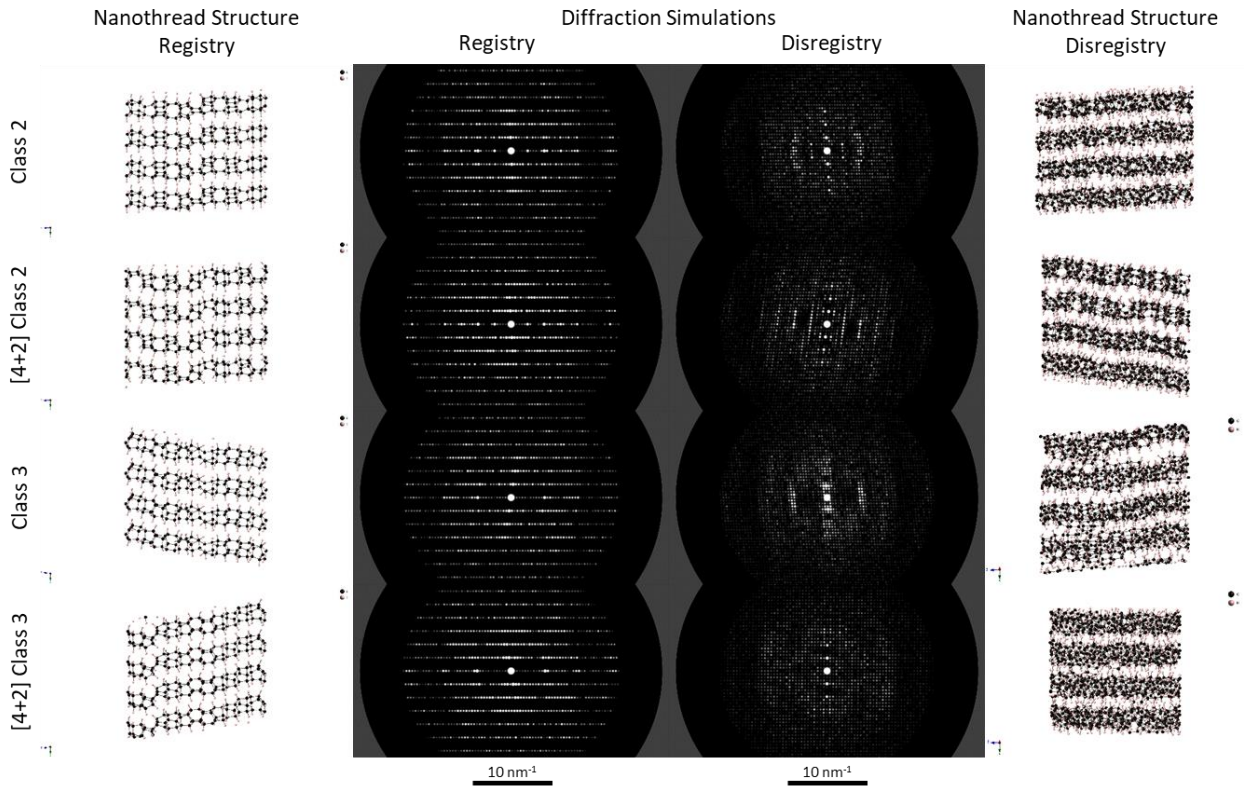

Figure S13. Simulated models and electron diffraction patterns viewing $[10\bar{1}0]$ of disordered class 2, [4+2] class 2, class 3, and [4+2] class 3 nanothreads with either packing registry or packing disregistry. These nanothread structures are on-thread disordered; each thread within a 4×4 supercell has identical on-thread disorder. Models with packing registry are included for completeness, but are not anticipated to be experimentally relevant since distinctly disordered threads cannot assume a packing registry. However, when packed with disregistry, even these highly-disordered models exhibit weak, diffuse layer lines due to the rough periodicity that remains in the placement of successive progenitor benzene-derived subunits. In particular, the class 2 species maintain a ···2/4/2/4/2/4··· periodicity in the number of covalent bonds between these subunits.

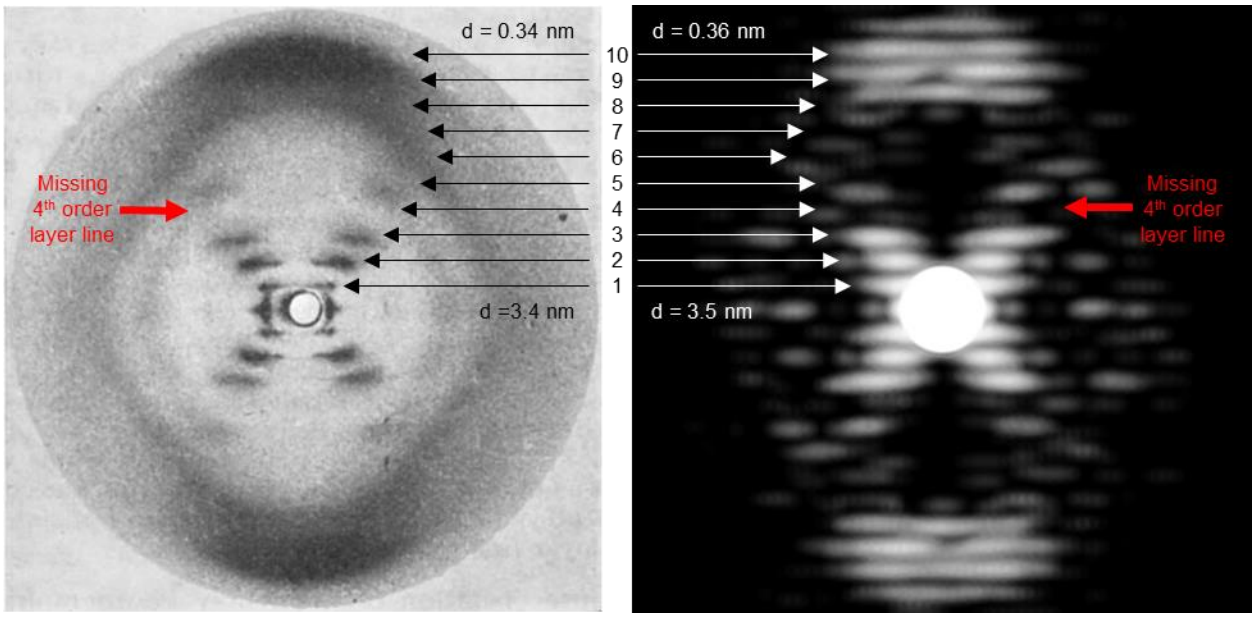

Figure S14. Comparison of the famous experimental x-ray pattern of B-DNA by Rosalind Franklin[8] (left) with a simulated electron diffraction pattern of B-DNA from the SingleCrystal™ software (right). The locations, intensities, and absences of the layer lines are similar between the experimental and simulated diffraction patterns, illustrating the origin of layer lines.

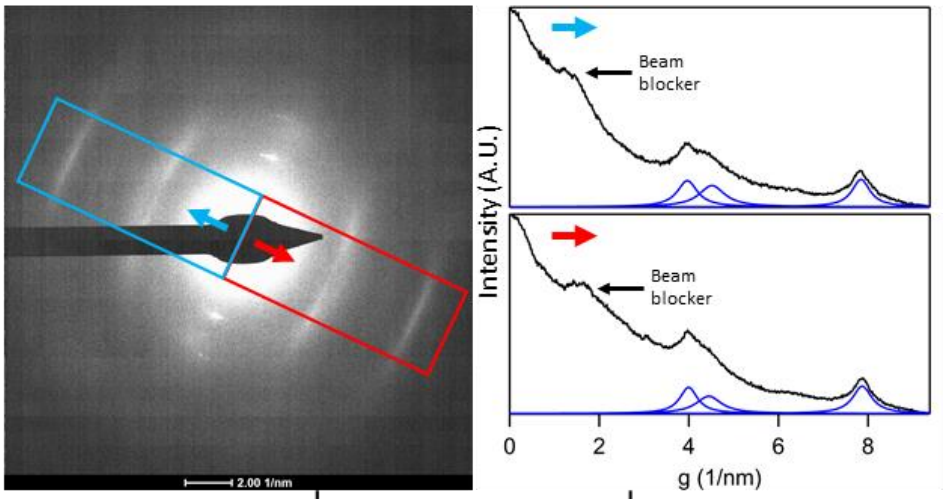

Layer Line Location		Layer Line FWHM		Nanothread Domain Length (D)	
1/nm	degrees	1/nm	degrees	nm	Average (nm)
3.96	0.29	0.54	0.04	1.6	**1.7**
4.51	0.32	0.70	0.05	1.3	**1.3**
7.84	0.56	0.49	0.04	1.8	**1.8**
3.99	0.29	0.48	0.03	1.8	
4.44	0.32	0.69	0.05	1.3	
7.87	0.52	0.52	0.04	1.7	

Figure S15. Estimation of nanothread domain length from the full-width at half-maximum (FWHM) of the electron diffraction layer lines from Figure 5b and Figure 5c. Lorentzian functions are fit to peaks in the linear intensity profiles (top right) of a nanothread electron diffraction pattern with layer lines (top left). The location and FWHM of the Gaussian peaks were used to estimate the nanothread domain length (D) by means of the Scherrer equation, $D = \frac{K\lambda}{\beta cos\theta}$ where K = shape factor (0.89), λ = relativistic wavelength of a 200-kV electron, β = 2 × FWHM (radians), and θ = location of peak (radians). The peak location and FWHM values are converted to scattering angles (θ in degrees) using Bragg's Law, $\theta = \sin^{-1}(q\lambda/2)$. The domain sizes of 1.3, 1.7, and 1.8 nm are associated with coherent lengths of different nanothread species existing in the sample. The 1.7–1.8 nm domain size is calculated for the two layer lines that have peak positions that are nearly exact multiples, which strongly suggests that they are associated with a single nanothread structure. These calculated domain sizes are considered a lower bound on the actual nanothread domain length. The ~4 nm^{-1} location of the most prominent layer line is consistent with those observed in diffraction simulations of nanothreads with packing disregistry, but the quality of the data is not sufficient to identify the specific thread structure at present.

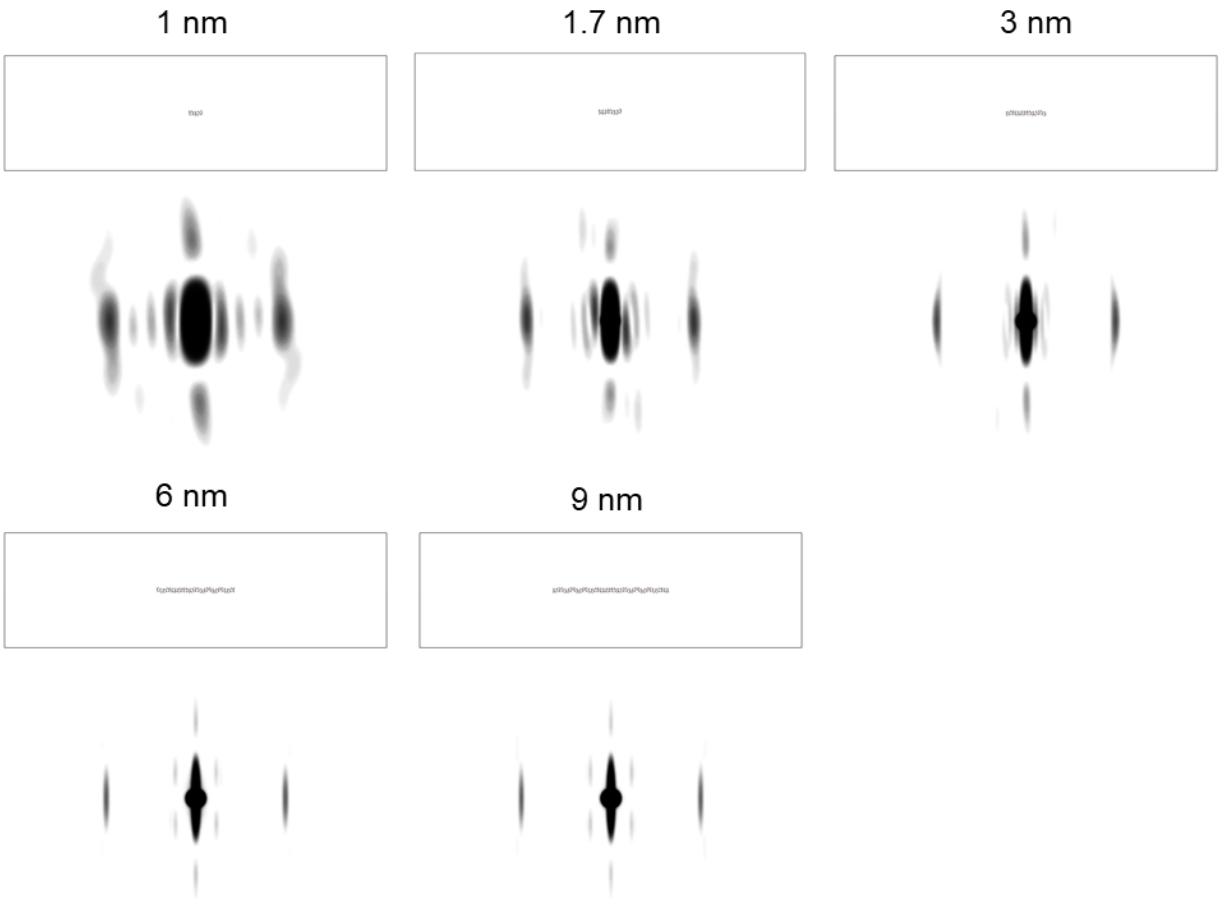

Length	1 nm	1.7 nm	3 nm	6 nm	9 nm
Location (2θ)	0.665	0.655	0.641	0.636	0.631
Max (2θ)	0.545	0.583	0.602	0.612	0.617
Min (2θ)	0.120	0.072	0.039	0.024	0.014
FWHM (2θ)	0.060	0.036	0.020	0.012	0.007
FWHM (θ)	**0.06**	**0.04**	**0.02**	**0.01**	**0.01**

Figure S16. Calculation of scattering from finite nanothreads of different lengths. We constructed models consisting of a largely empty 9×9×30 nm cubic unit cells into which ordered, stiff-chiral-3 (13$\underline{64}$25) nanothreads of various lengths were placed. The ends of these finite-length threads are meant to represent a loss of translational order – in a longer thread this effect would be caused by e.g. point defects that disrupt translational order. The largely empty unit cell allows simulation that requires a repeating cell (as in SingleCrystal™) to approximate an isolated domain (or a collection of such domains not symmetry-related to each other). The FWHMs of the layer lines are then approximated by the horizontal widths of the diffraction streaks and are found to scale inversely with nanothread length, as anticipated. We obtain good agreement with the coherence length estimates from Scherrer's equation (Figure S15).

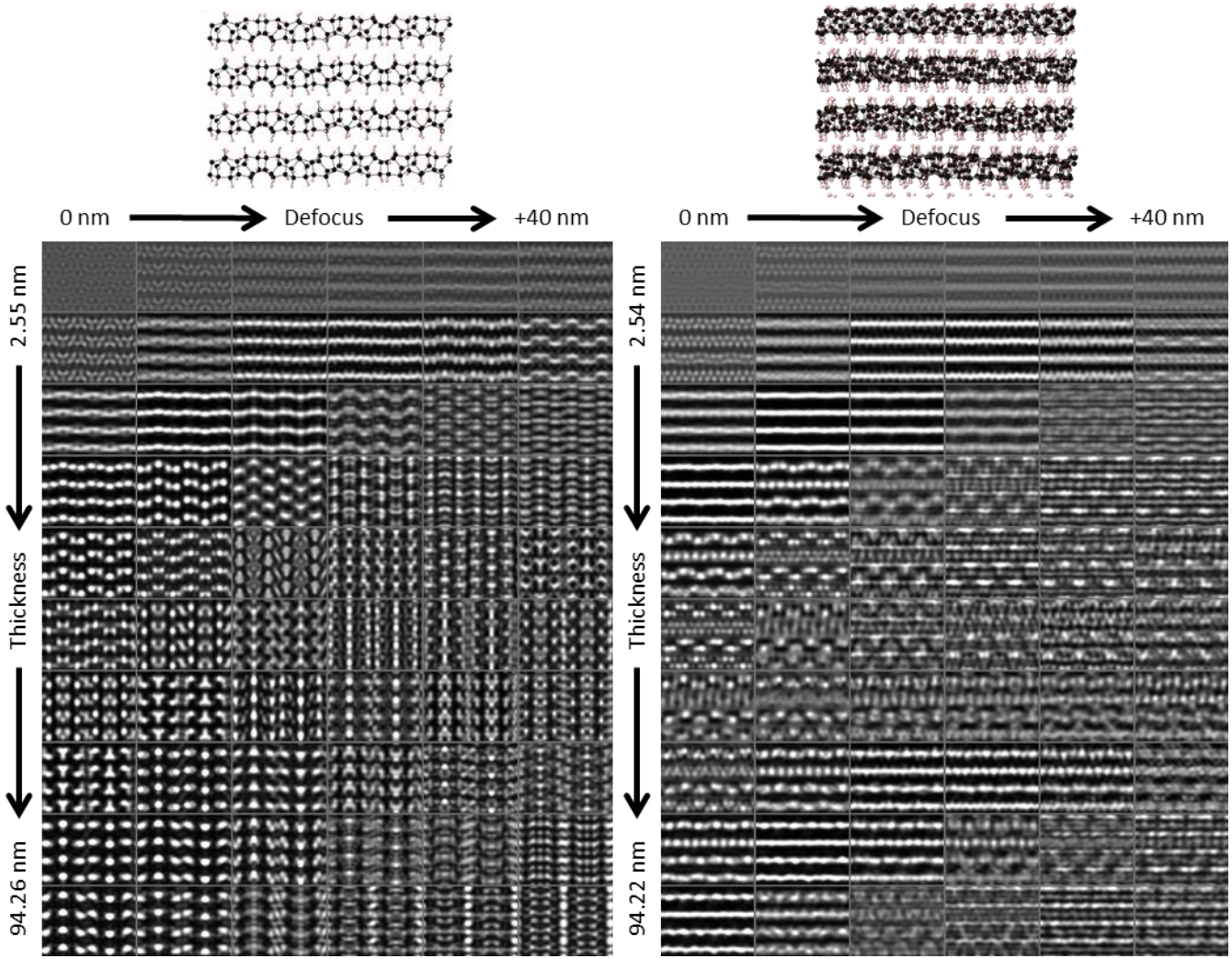

Figure S17. Rendered real-space models and montages of TEM image simulations of polytwistane (14̲36̲52) nanothreads in the [10$\bar{1}$0] orientation with packing registry (left) and packing disregistry (right) over a range of thickness up to ~100 nm and defocus values 0–40 nm. Disregistered simulations in Figures S17–S26 are constructed from sufficient repeats of the 4×4×y supercell (y=1 for threads with Z>6, otherwise y=3, where Z is the number of progenitor benzene rings in the unit cell) make up the thickness of the simulated sample. This introduces an artificial registry on the scale of the supercell dimension which is removed in the extended-cell simulations of Figure S31.

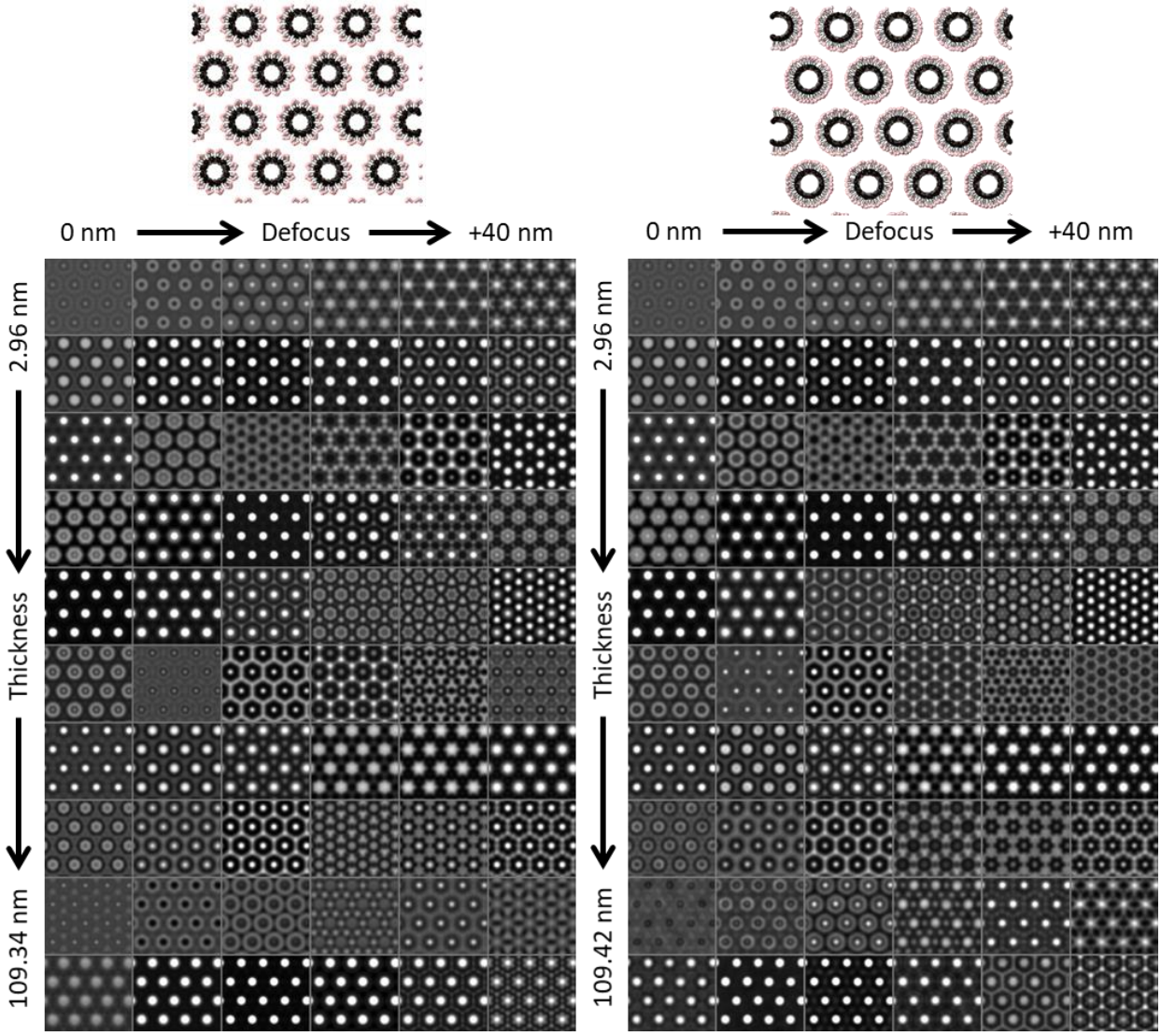

Figure S18. Molecular models and montages of TEM image simulations of polytwistane (143652) nanothreads in the [0001] orientation with packing registry (left) and packing disregistry (right) over a range of thickness up to ~100 nm and defocus values 0–40 nm.

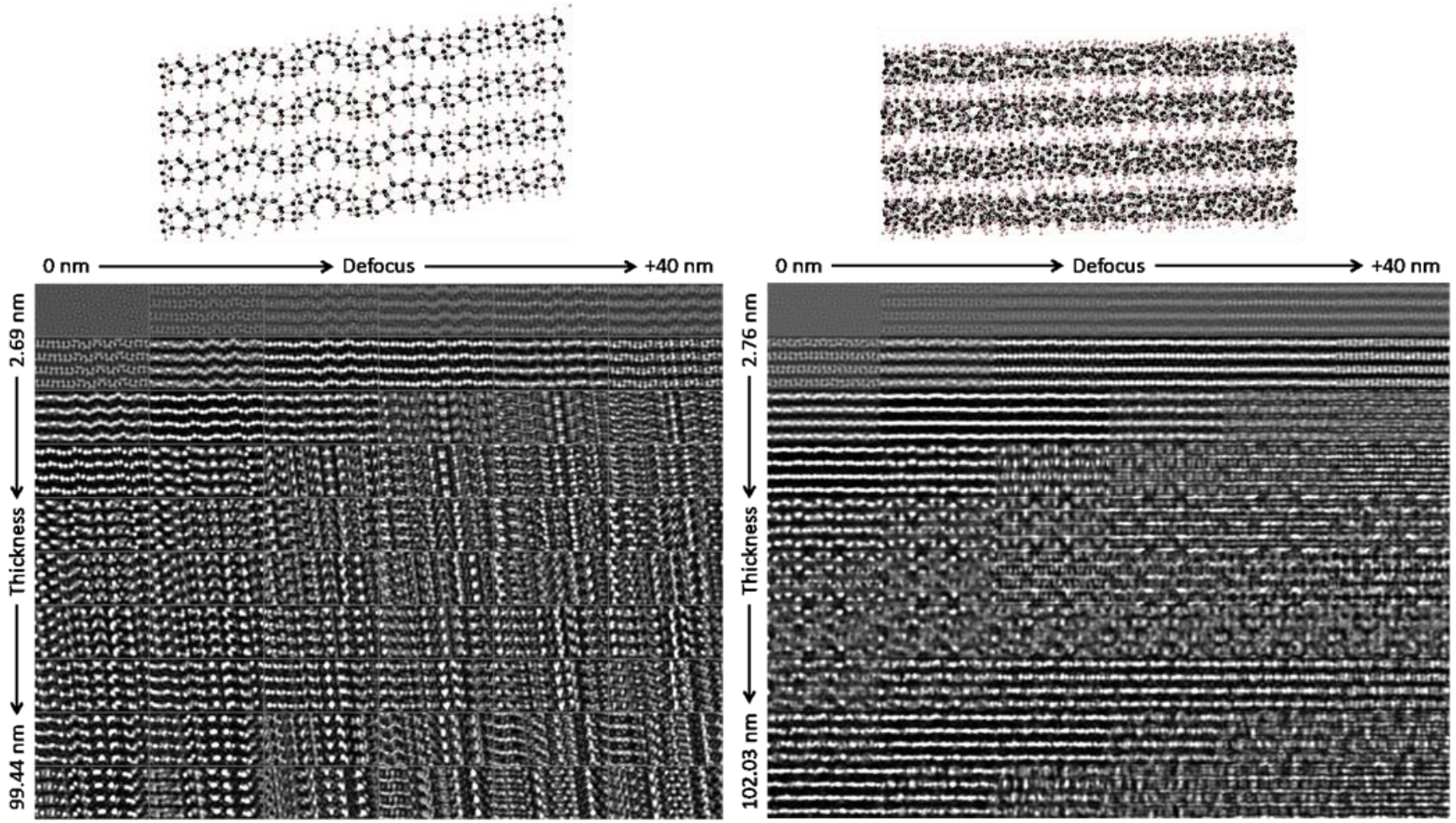

Figure S19. Molecular models and montages of TEM image simulations of stiff-chiral-3 (13$\underline{6}$4$\underline{2}$5) nanothreads in the [10$\bar{1}$0] orientation with packing registry (left) and packing disregistry (right) over a range of thickness up to ~100 nm and defocus values 0–40 nm.

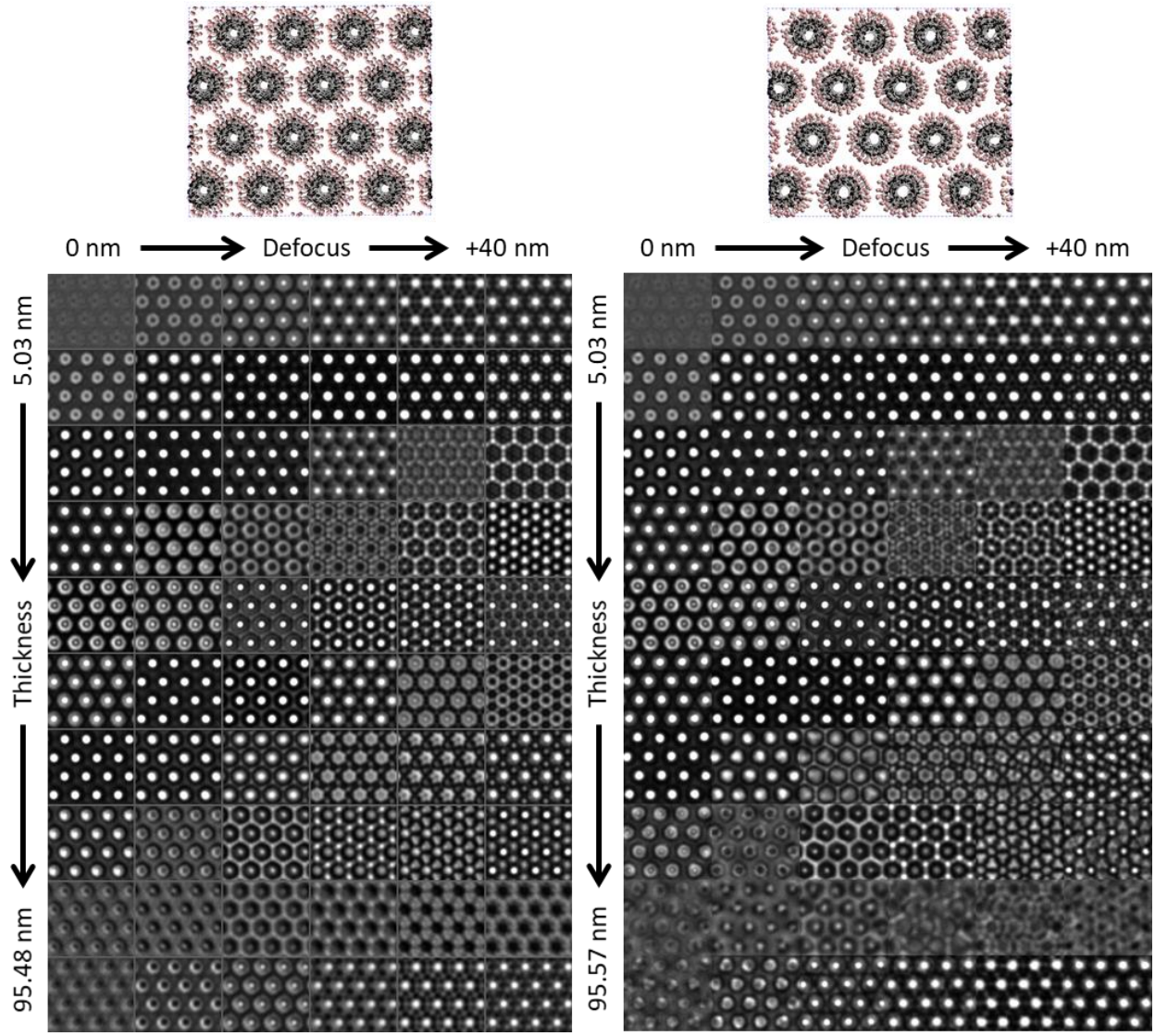

Figure S20. Molecular models and montages of TEM image simulations of stiff-chiral-3 (13$\underline{6}$4$\underline{2}$5) nanothreads in the [0001] orientation with packing registry (left) and packing disregistry (right) over a range of thickness up to ~100 nm and defocus values 0–40 nm.

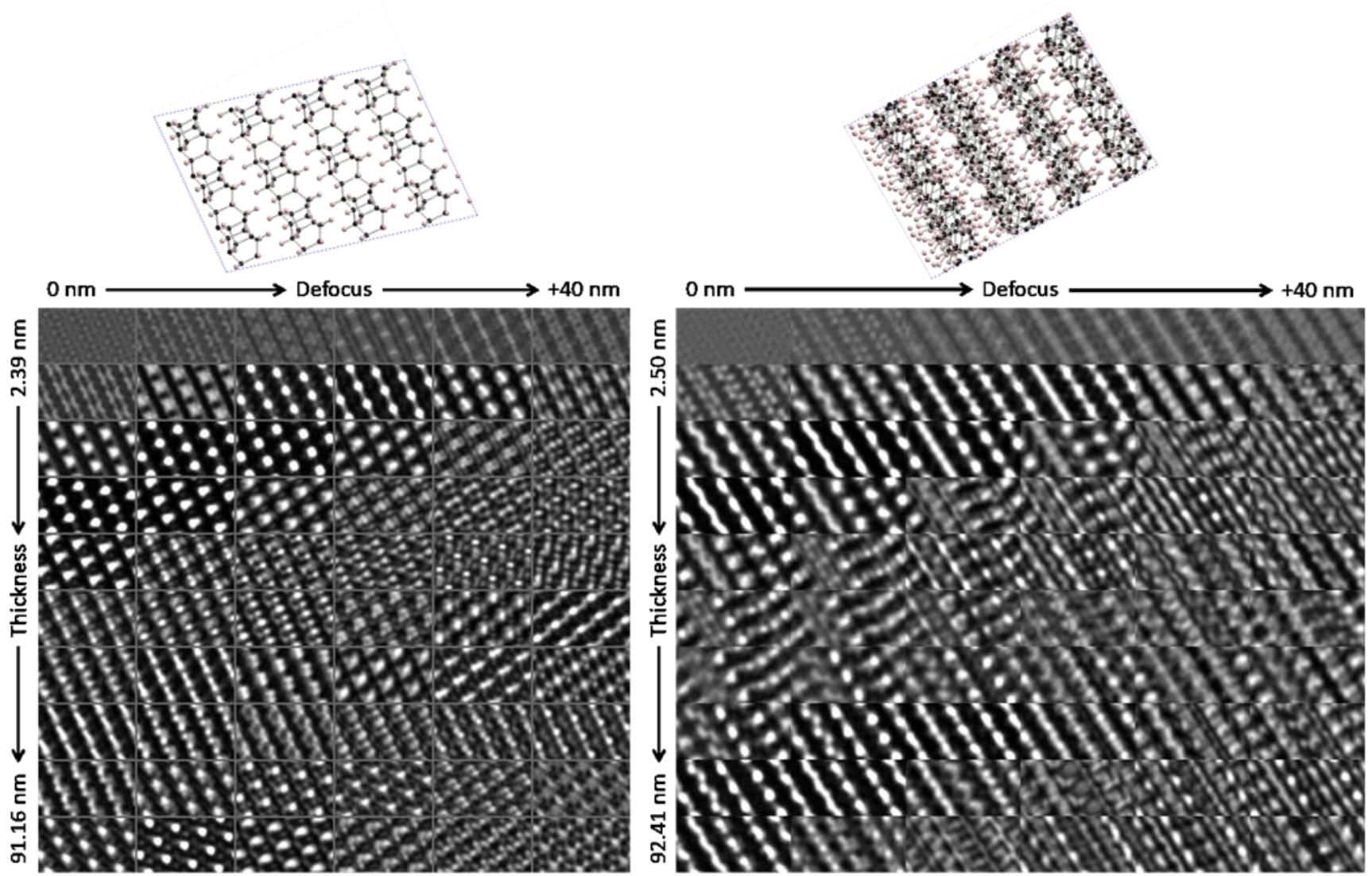

Figure S21. Molecular models and montages of TEM image simulations of square polymer (14̲3562) nanothreads in the [10$\bar{1}$0] orientation with packing registry (left) and packing disregistry (right) over a range of thickness up to ~100 nm and defocus values 0–40 nm.

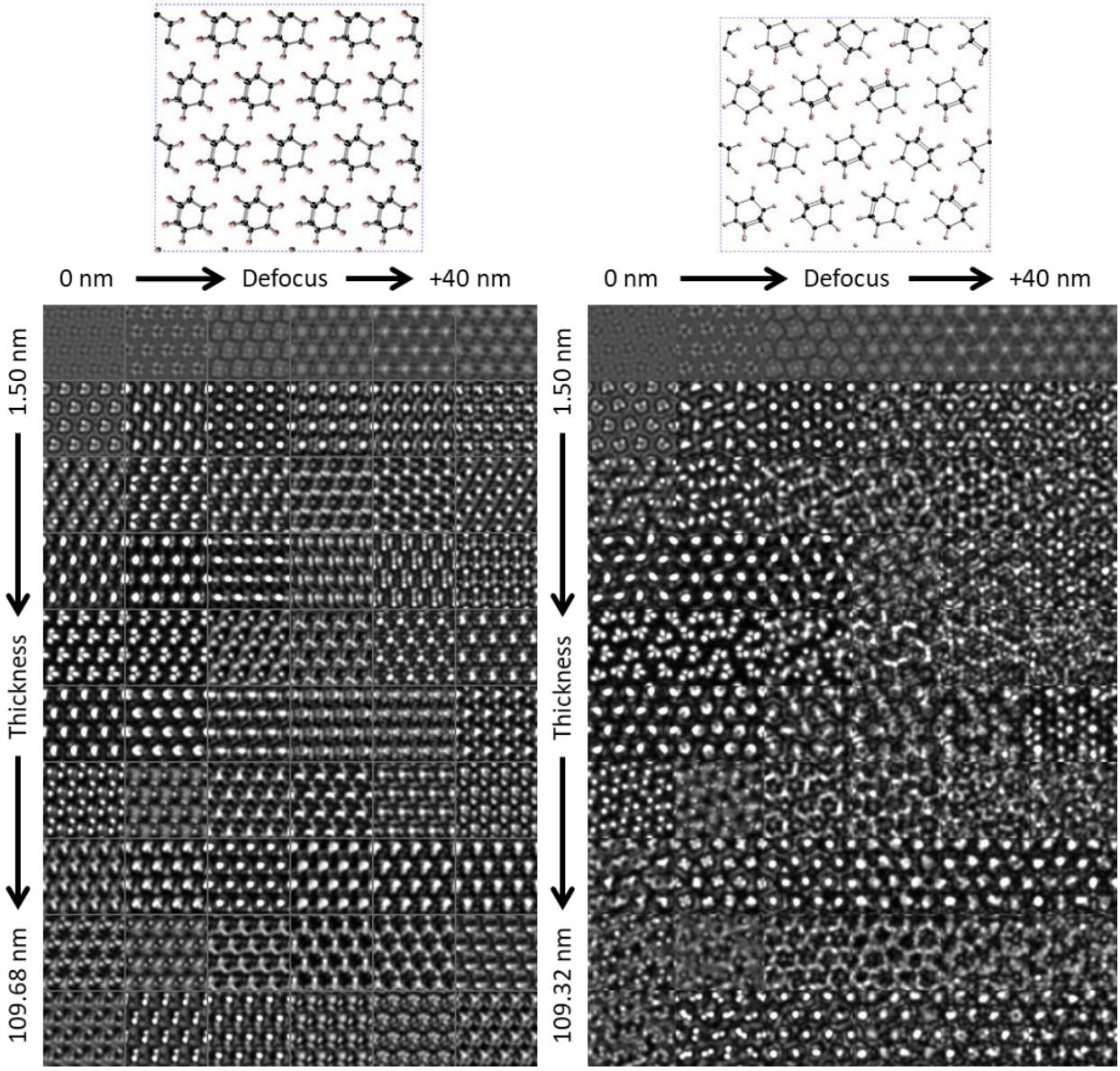

Figure S22. Molecular models and montages of TEM image simulations of square polymer (143562) nanothreads in the [0001] orientation with packing registry (left) and packing disregistry (right) over a range of thickness up to ~100 nm and defocus values 0–40 nm.

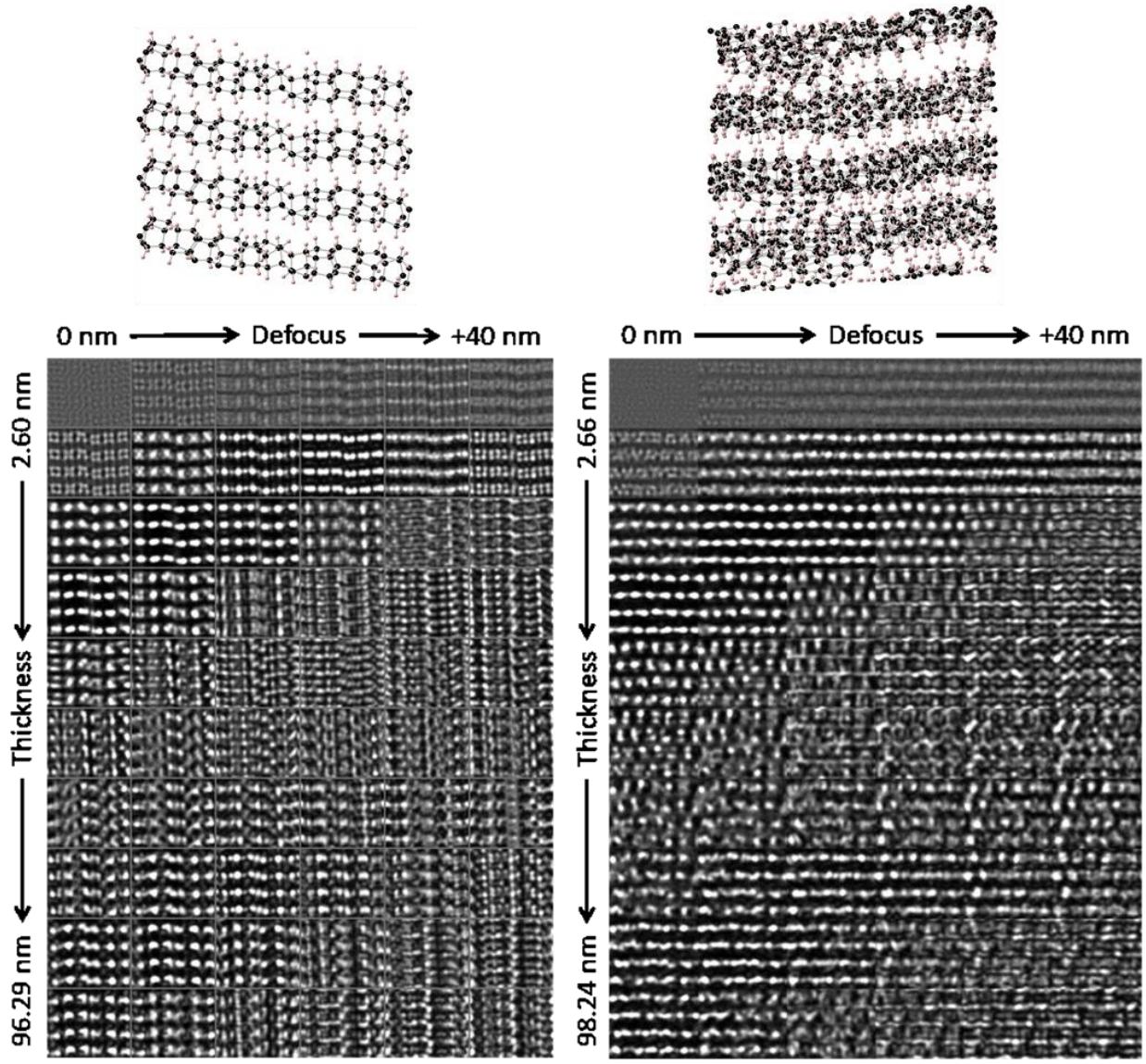

Figure S23. Molecular models and montages of TEM image simulations of disordered class 2 nanothreads in the $[10\bar{1}0]$ orientation with packing registry (left) and packing disregistry (right) over a range of thickness up to ~100 nm and defocus values 0–40 nm. Packing registry of an on-thread-disordered system is not likely to occur in experiment.

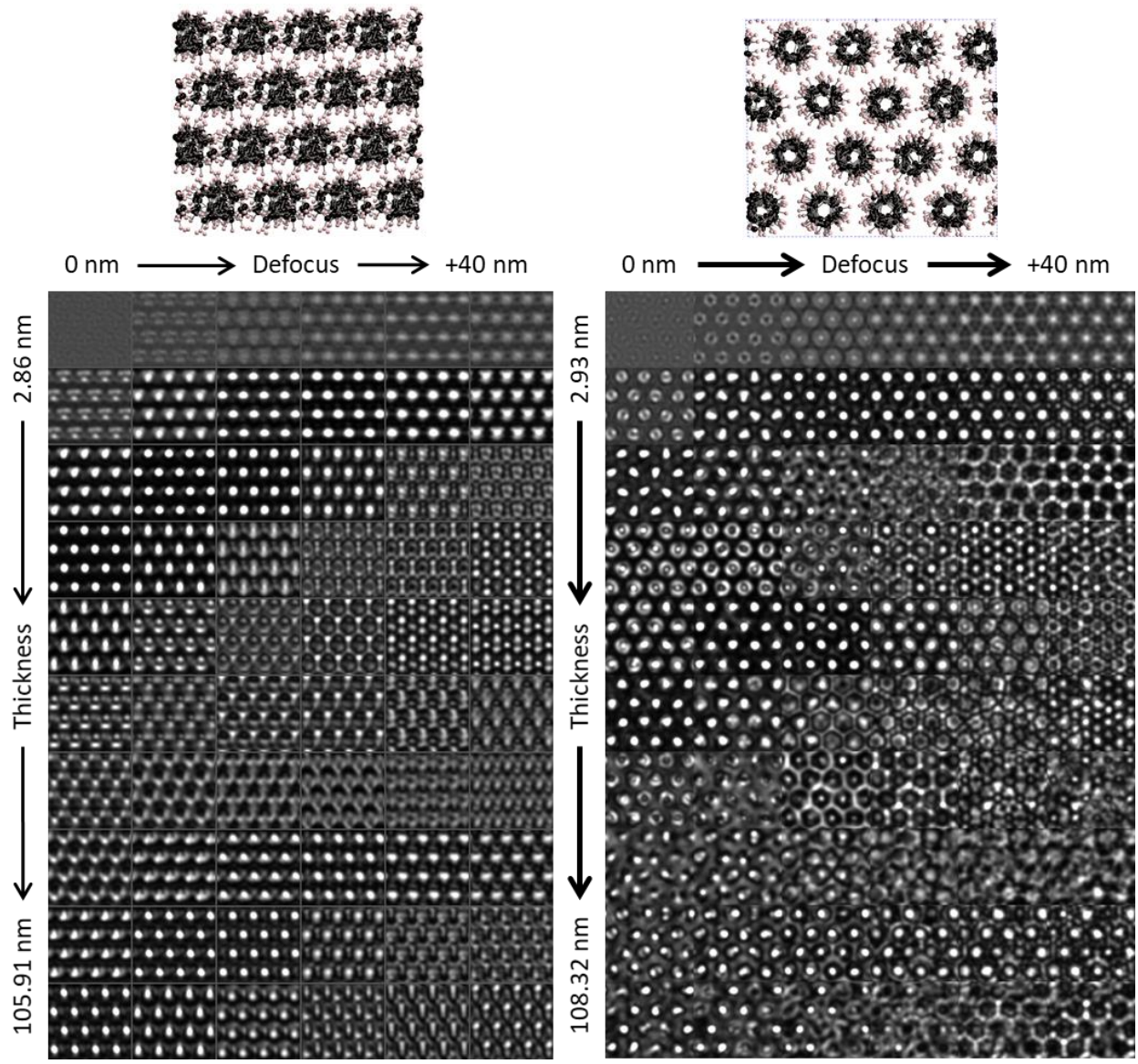

Figure S24. Molecular models and montages of TEM image simulations of disordered class 2 nanothreads in the [0001] orientation with packing registry (left) and packing disregistry (right) over a range of thickness up to ~100 nm and defocus values 0–40 nm.

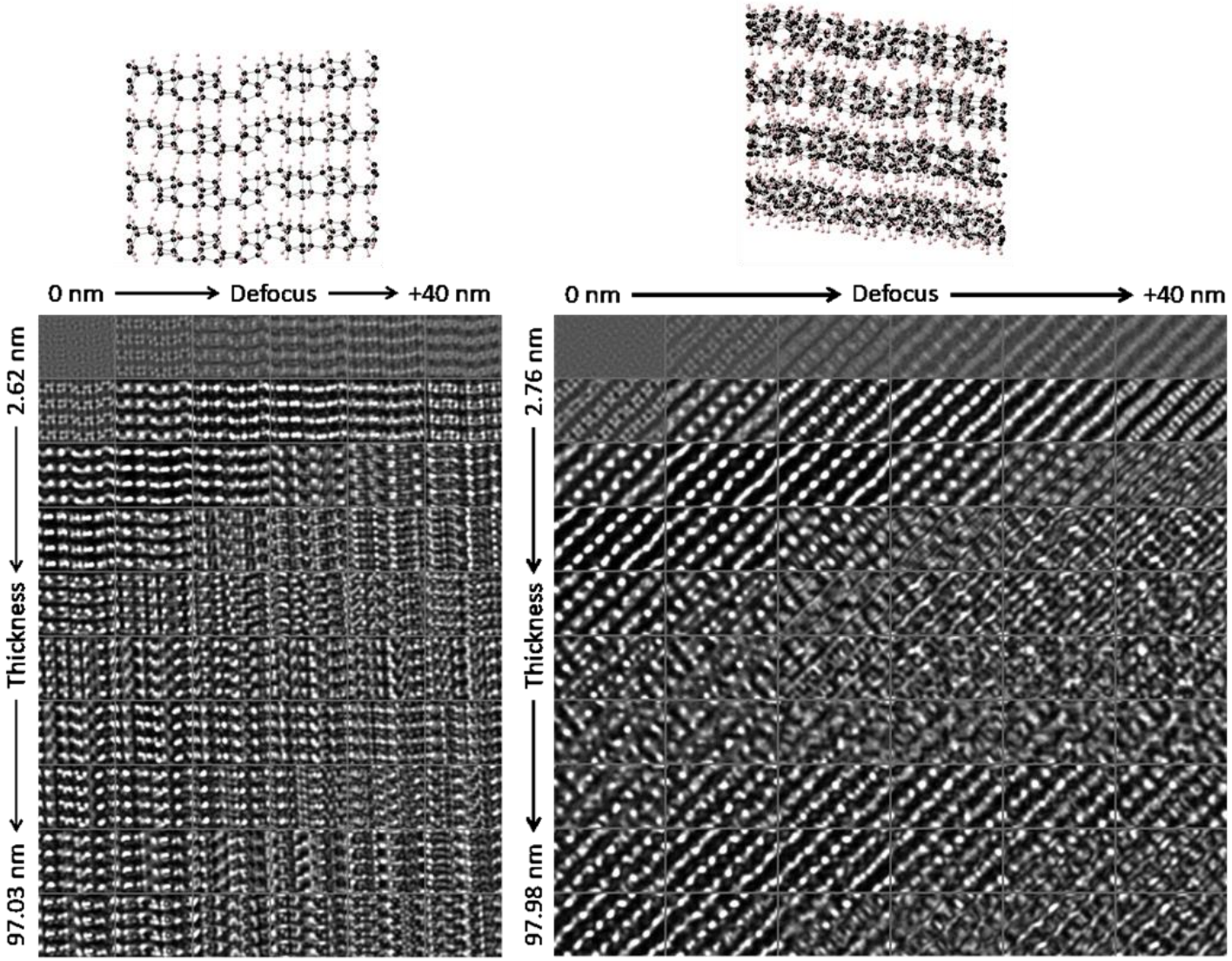

Figure S25. Molecular models and montages of TEM image simulations of disordered [4+2] class 2 nanothreads in the [10$\bar{1}$0] orientation with packing registry (left) and packing disregistry (right) over a range of thickness up to ~100 nm and defocus values 0–40 nm.

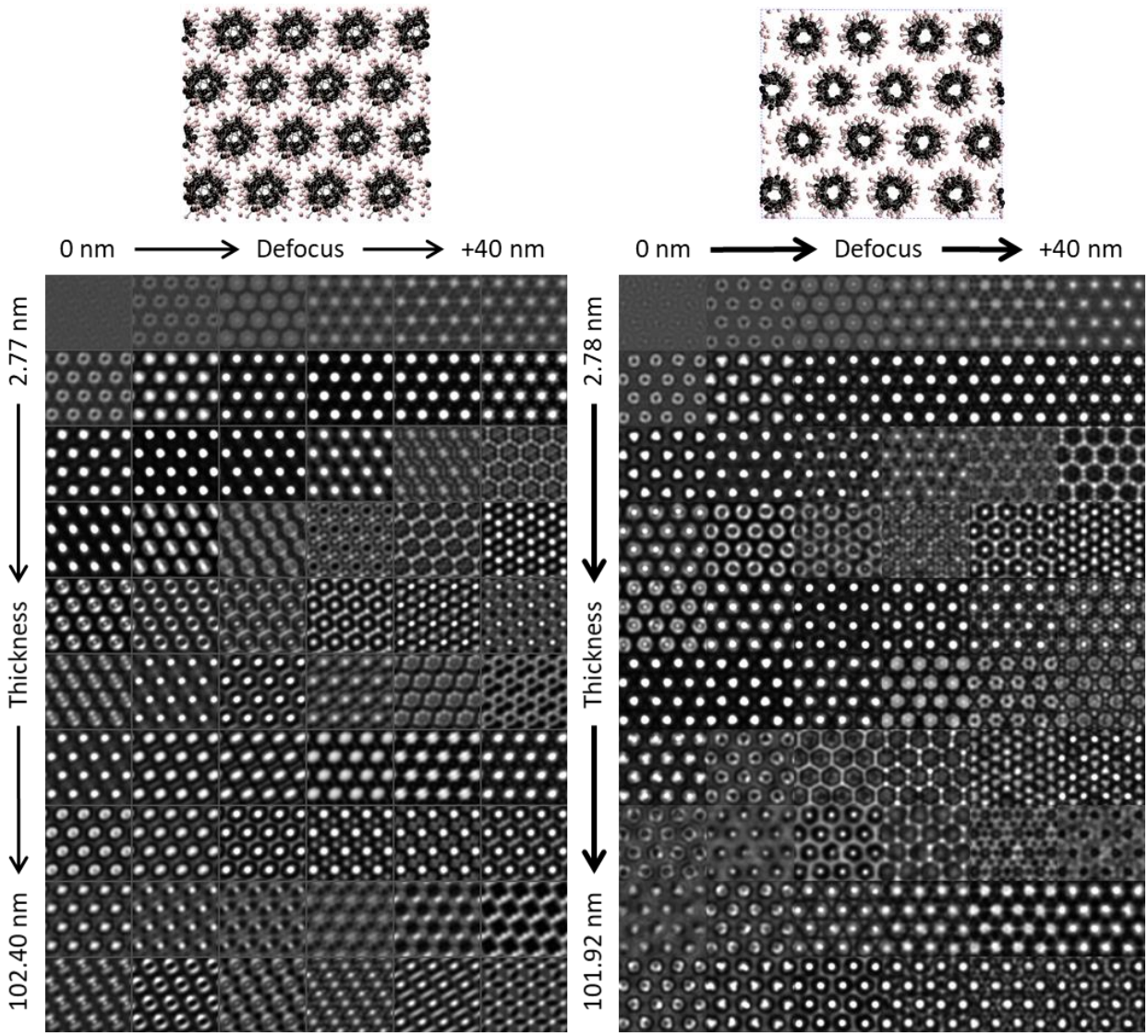

Figure S26. Molecular models and montages of TEM image simulations of disordered [4+2] class 2 nanothreads in the [0001] orientation with packing registry (left) and packing disregistry (right) over a range of thickness up to ~100 nm and defocus values 0–40 nm.

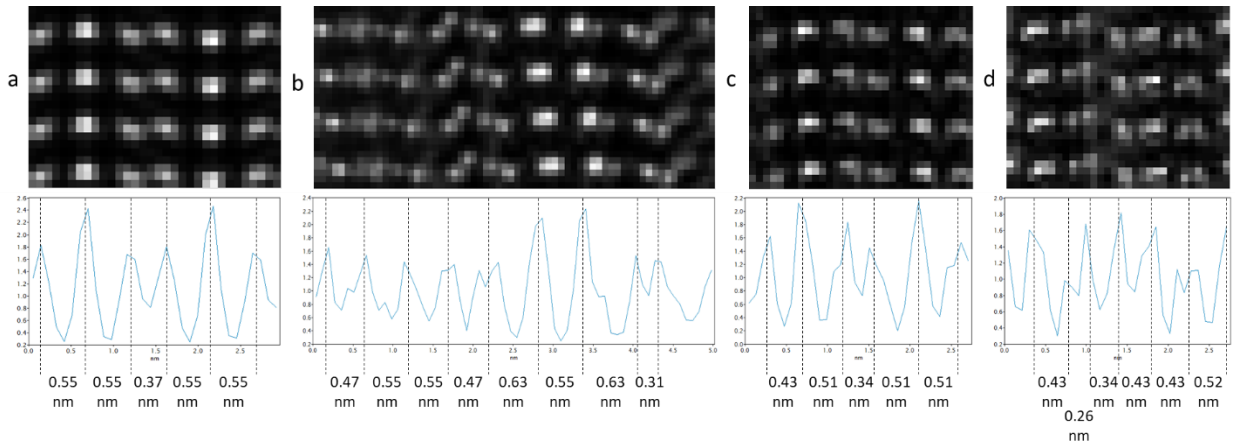

Figure S27. TEM image simulations and line profiles parallel to the thread axis of (a) polytwistane (14$\underline{3}$6$\underline{5}$2), (b) stiff-chiral-3 (13$\underline{6}$4$\underline{2}$5), (c) class–2, and (d) 4+2 class–2 nanothreads with ordered packing in the [10$\bar{1}$0] orientation. The simulated images have similar thickness in the range of 84–89 nm (with supercell repeats to make up the full thickness as discussed earlier), defocus of +8 nm, and have been binned to ~1 Å^2 pixel size to match the pixel size of the experimental images (Figures S32–S34) as closely as possible. The distance seen between beads in these simulations has a mean and standard deviation of 0.5 ± 0.1 nm, ranging from 0.26 to 0.63 nm.

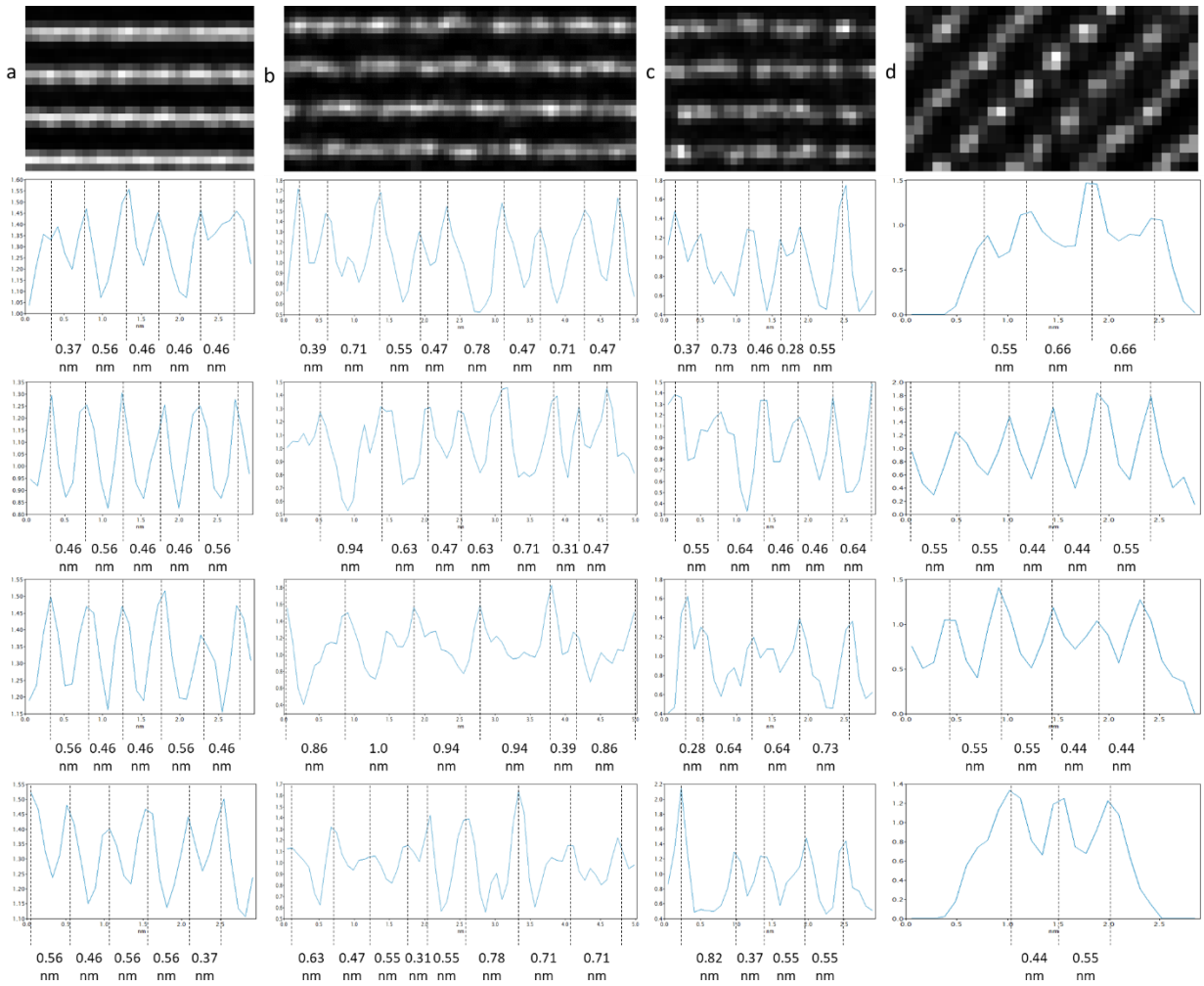

Figure S28. TEM image simulations and line profiles of (a) polytwistane (14$\underline{3}$6$\underline{5}$2), (b) stiffchiral-3 (13$\underline{6}$4$\underline{2}$5), (c) class–2, and (d) 4+2 class–2 nanothreads with disordered packing in the [10$\bar{1}$0] orientation. The simulated images have similar thicknesses in the range of 84–91 nm (with supercell repeats to make up the full thickness), defocus of +8 nm, and have been binned to ~1 Å^2 pixel size to match the pixel size of the experimental images (Figures S32–S34) as closely as possible. Each row of line profile measurements represents each of the four columns of nanothreads in the simulated images which have unique and distinct beading due to packing disregistry. Packing disregistry yields a broader range of inter-bead spacings, with mean and standard deviation of 0.6 ± 0.2 nm ranging from 0.28 nm to 1.0 nm.

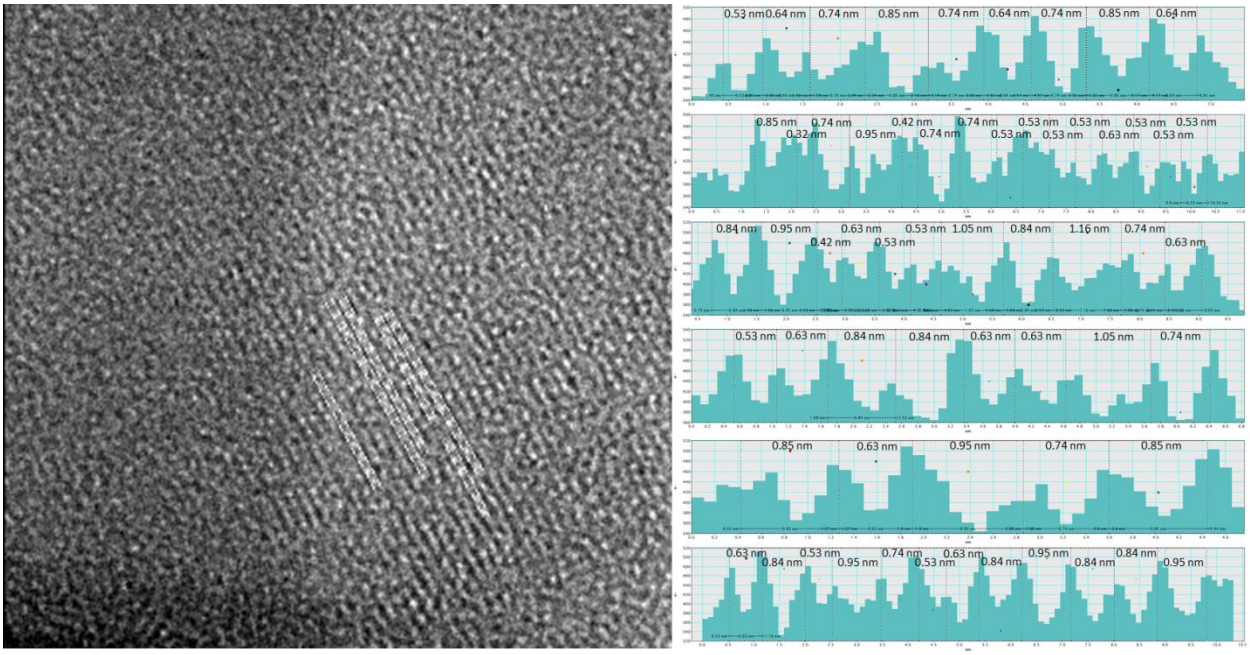

Figure S29. Line profile measurements (white boxes) of inter-bead spacing in a HREM image of nanothreads (from Figure 6c). The distances measured between beads are typically 0.7 ± 0.2 nm with a maximum of 1.16 nm and a minimum of 0.42 nm. These inter-bead spacings in the experimental images (such as shown in Figure S30) are in better agreement with the inter-bead distances measured from TEM image simulations of nanothreads in packing disregistry rather than registry.

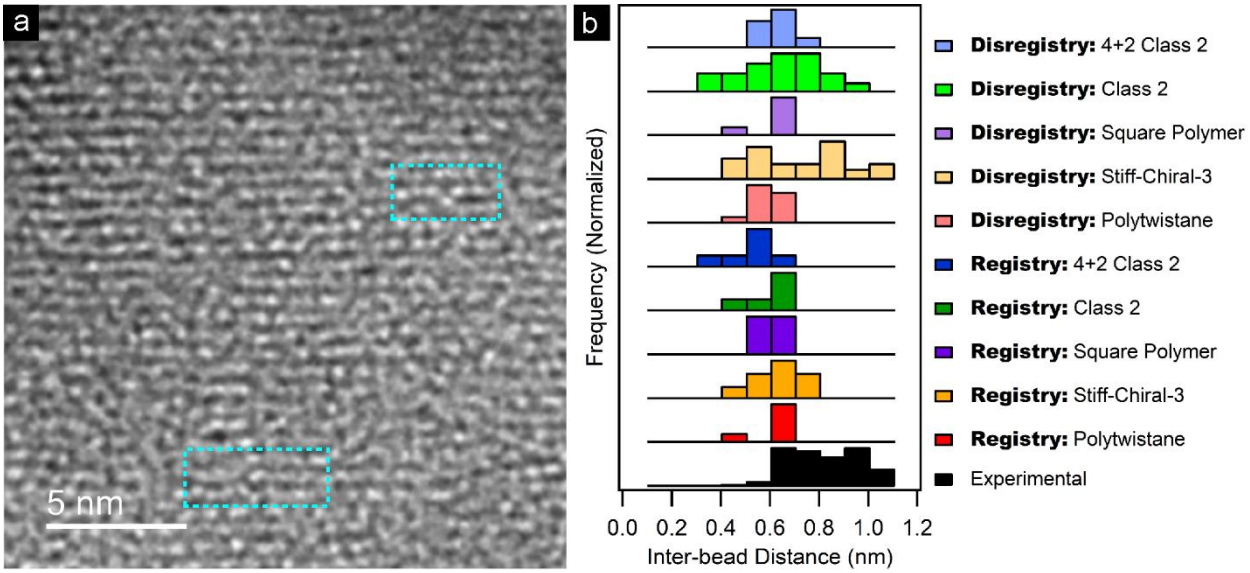

Figure S30. A magnified HREM image shows distinct beading in the nanothread packing (a). The HREM image was linearly interpolated to decrease the pixel size to ~10 pm^2 to match the pixel resolution of TEM image simulations of nanothreads. The blue boxes indicate areas with what appear to be localized defects; in the lower case, a possible dislocation. Histograms (b) compare the inter-bead distances in the experimental image with inter-bead distances of TEM image simulations of [10$\bar{1}$0] nanothreads with packing disregistry or registry, and with or without on-thread disorder (based on results depicted in Figures S27–S29). The distribution of experimental inter-bead distances is best fit by stiff-chiral-3 nanothreads with packing disregistry, but the data do not afford a precise identification, due to the inherent breadth of the distributions and uncertainties in thread structure and the possibility of mixed thread populations.

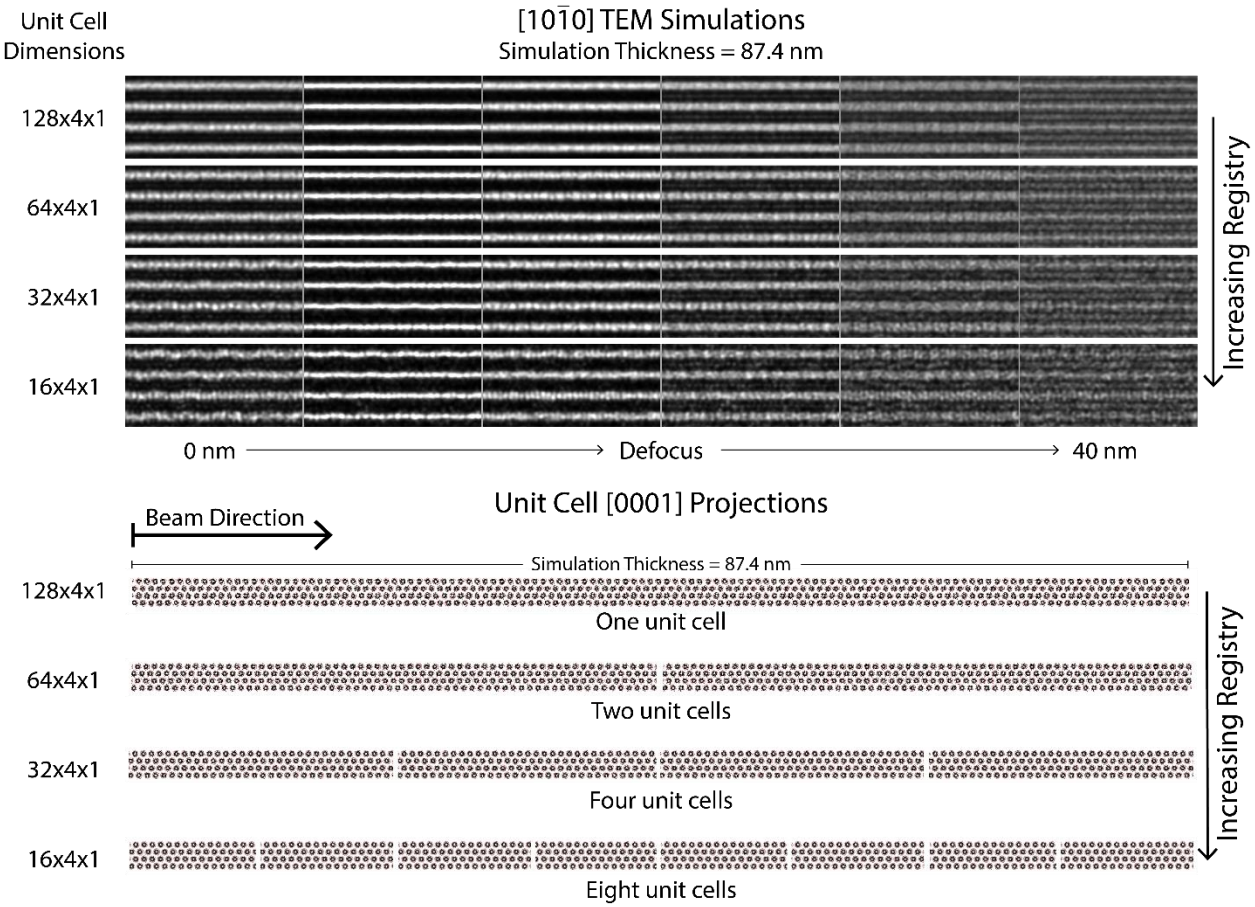

Figure S31. Comparison of TEM image simulations (simulation thickness = 87.4 nm, defocus = 0–40 nm) of stiff-chiral-3 nanothreads with packing disregistry and varying supercell dimensions. Whereas the earlier disregistered image simulations constructed the sample thickness by repeats of 4×4×y disordered supercell, this image sequence uses much thicker disregistered supercells that can reach the full width of 87.4 nm for the 128×4×1 supercell, with each individual thread at a unique axial/azimuthal offset. These image simulations control for the effect of supercell repeats at a constant simulation thickness (i.e. the smallest supercell is stacked 8 times to reach 87.4-nm thickness whereas the largest supercell achieves this thickness with no repeats). More complete disregistry weakens the beading contrast but does not eliminate it in simulations comparable to the thickness of the nanothread particle examined experimentally. These simulations establish that the experimental observation of beading cannot be used to determine the degree of registry between adjacent threads. For reason of computational cost, the disregistered supercells used here were constructed statically, i.e. relaxed as individual threads but without interthread structural relaxation.

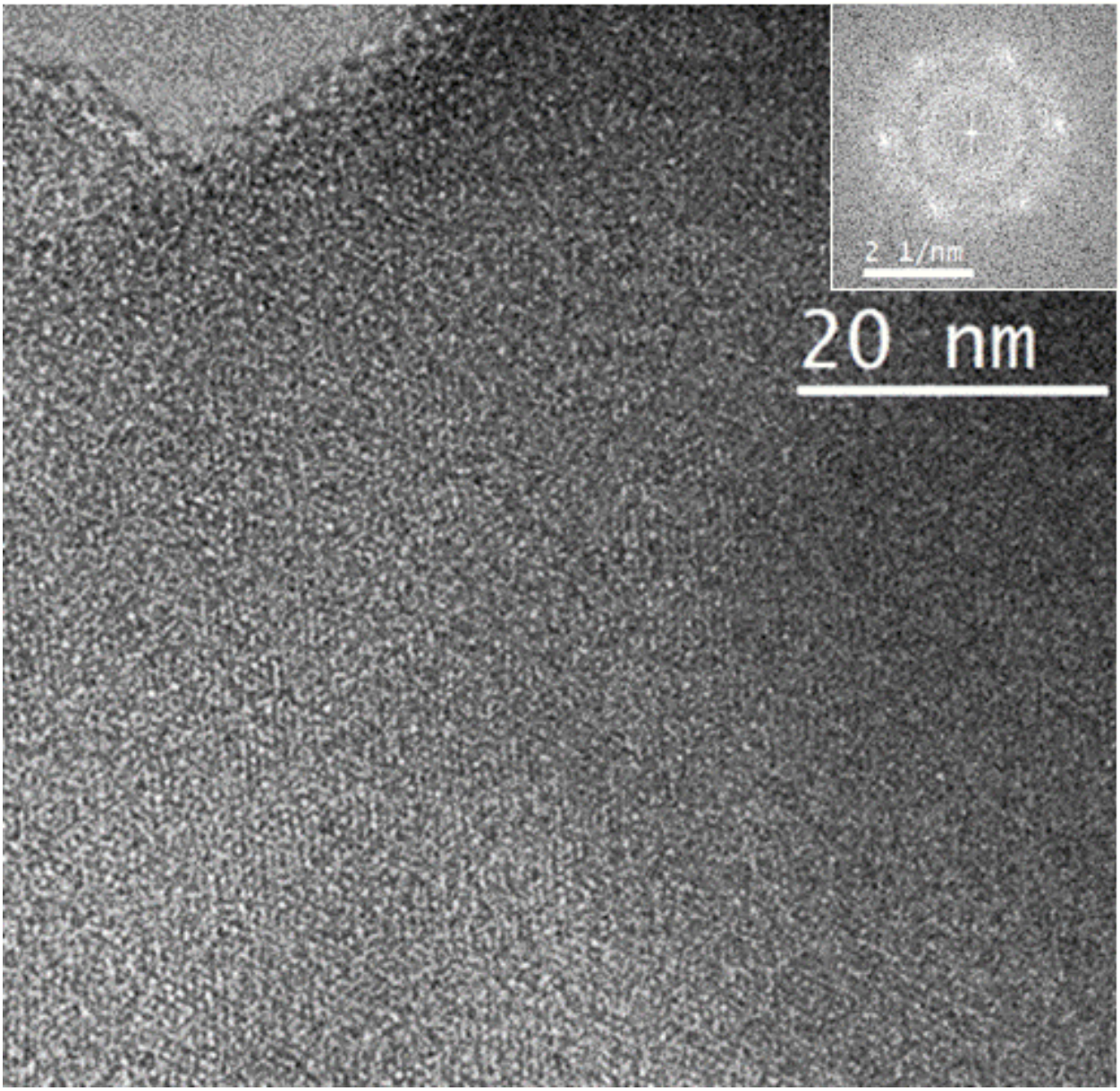

Figure S32. HREM image of nanothreads in the [0001] orientation with inset FT of the image. A cropped area of this image is shown in Figure 4d. The mottled pattern in the image and the six-fold spots in the FT suggest a near end-on orientation for the nanothread lattice across the field-of-view, with modest variations in axial direction.

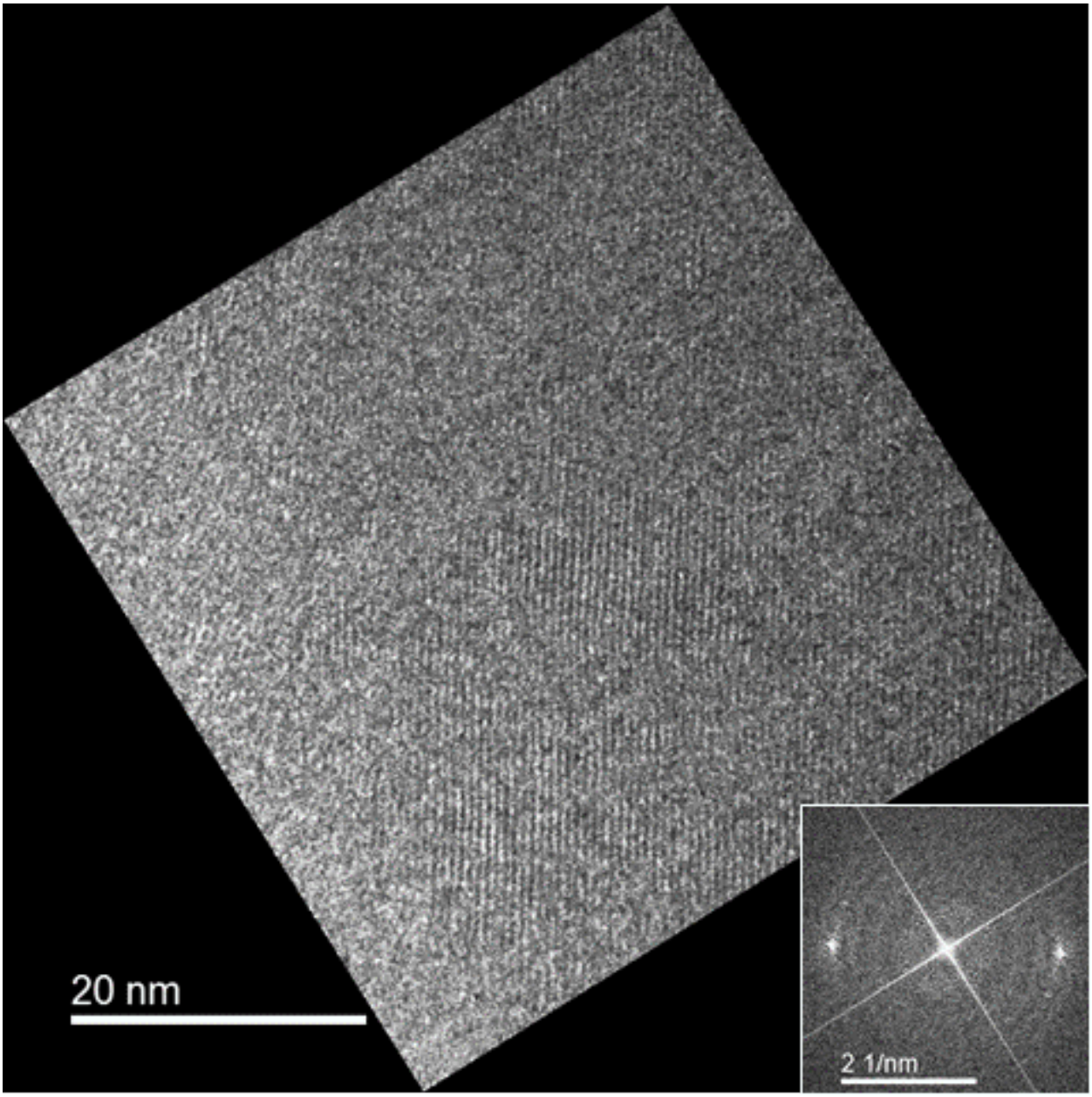

Figure S33. HREM image of nanothreads from an orientation off [0001] with inset FT of the image. The image is rotated by 32° in the clockwise direction to orient in the vertical direction the nanothreads in the bottom corner of the image. A cropped area of this image is shown in Figure 6.

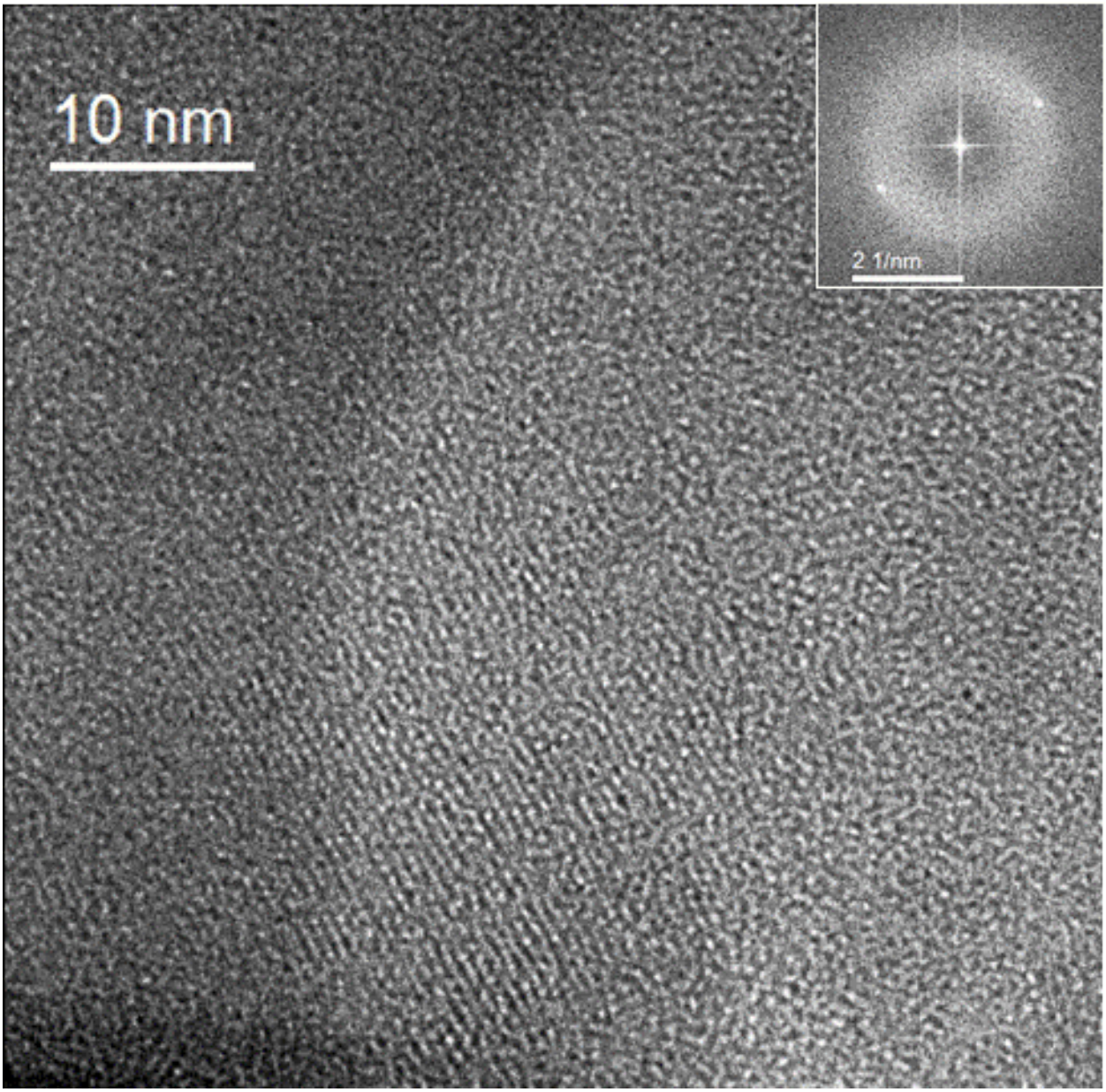

Figure S34. HREM image of nanothreads from an orientation off [0001] with inset FT of the image. Cropped areas of this image are shown in Figures S29–S30.

References

(1) Mitchell, D. R.; Schaffer, B. Scripting-Customized Microscopy Tools for Digital Micrograph. *Ultramicroscopy* **2005,** *103*, 319-32.

(2) Schindelin, J.; Arganda-Carreras, I.; Frise, E.; Kaynig, V.; Longair, M.; Pietzsch, T.; Preibisch, S.; Rueden, C.; Saalfeld, S.; Schmid, B.; Tinevez, J. Y.; White, D. J.; Hartenstein, V.; Eliceiri, K.; Tomancak, P.; Cardona, A. Fiji: An Open-Source Platform for Biological-Image Analysis. *Nat. Methods* **2012,** *9*, 676-82.

(3) Xu, E. S.; Lammert, P. E.; Crespi, V. H. Systematic Enumeration of sp^3 Nanothreads. *Nano Lett.* **2015,** *15*, 5124-30.

(4) Cornell, W. D.; Cieplak, P.; Bayly, C. I.; Gould, I. R.; Merz, K. M.; Ferguson, D. M.; Spellmeyer, D. C.; Fox, T.; Caldwell, J. W.; Kollman, P. A. A Second Generation Force Field for the Simulation of Proteins, Nucleic Acids, and Organic Molecules. *J. Am. Chem. Soc.* **1996,** *118*, 2309-2309.

(5) Plimpton, S. Fast Parallel Algorithms for Short-Range Molecular Dynamics. *J. Comput. Phys.* **1995,** *117*, 1-19.

(6) Wang, T.; Duan, P.; Xu, E. S.; Vermilyea, B.; Chen, B.; Li, X.; Badding, J. V.; Schmidt-Rohr, K.; Crespi, V. H. Constraining Carbon Nanothread Structures by Experimental and Calculated Nuclear Magnetic Resonance Spectra. *Nano Lett.* **2018,** *18*, 4934-4942.

(7) Li, X.; Baldini, M.; Wang, T.; Chen, B.; Xu, E. S.; Vermilyea, B.; Crespi, V. H.; Hoffmann, R.; Molaison, J. J.; Tulk, C. A.; Guthrie, M.; Sinogeikin, S.; Badding, J. V. Mechanochemical Synthesis of Carbon Nanothread Single Crystals. *J. Am. Chem. Soc.* **2017,** *139*, 16343-16349.

(8) Franklin, R. E.; Gosling, R. G. Molecular Configuration in Sodium Thymonucleate. *Nature* **1953,** *171*, 740-1.